

Article

Synthesis, Characterization of Dy₂NdSbO₇/Bi₂WO₆ Heterojunction Photocatalyst and the Application for the Photocatalytic Degradation of Chlorpyrifos under Visible Light Irradiation

Jingfei Luan ^{1,2,*} , Liang Hao ¹, Ye Yao ¹ , Yichun Wang ¹, Guangmin Yang ¹ and Jun Li ¹

¹ School of Physics, Changchun Normal University, Changchun 130032, China; hliang0725@163.com (L.H.); yaoye1109@mails.jlu.edu.cn (Y.Y.); yichun2000@126.com (Y.W.); yangguangmin@ccsfu.edu.cn (G.Y.); 18043182231@163.com (J.L.)

² State Key Laboratory of Pollution Control and Resource Reuse, School of the Environment, Nanjing University, Nanjing 210093, China

* Correspondence: jfluan@nju.edu.cn; Tel.: +86-19951939498

Abstract: A groundbreaking photocatalytic nanomaterial, Dy₂NdSbO₇, was fabricated smoothly using the hydrothermal synthesis technique for the first time. Apart from that, Dy₂NdSbO₇/Bi₂WO₆ heterojunction photocatalyst (DBHP) was initially fabricated using the solvothermal fabrication technique. X-ray diffractometer, Fourier-transform infrared spectrometer, Raman spectrometer, UV-visible spectrophotometer, X-ray photoelectron spectrometer, inductively coupled plasma optical emission spectrometer, transmission electron microscope, and X-ray energy dispersive spectroscopy have been applied to evaluate and investigate the thetastructure, morphology, and physicochemical properties of synthesized samples. The results confirmed that the pyrochlore-type crystal structures of Dy₂NdSbO₇ belonged to the Fd3m space group with the cubic crystal system and the β-pyrochlore-type crystal structures of Bi₂WO₆ which belonged to the Pca21 space group with orthorhombic crystal system. Under visible light exposure for 155 min (VLP-155min) using DBHP in the capacity of the photocatalytic nanomaterial, the removal efficiency of chlorpyrifos (CPS) saturation reached 100%. Comparison of CPS removal efficiency after VLP-155min revealed that DBHP exhibited higher removal efficiency than Dy₂NdSbO₇, Bi₂WO₆, or N-doped TiO₂ photocatalyst, with removal efficiency 1.15 times, 1.23 times, or 2.55 times higher, respectively. Furthermore, the oxidizing capability of free radicals was investigated using trapping agents. Results demonstrated that superoxide anions exhibited the strongest oxidative capability, followed by hydroxyl radicals and holes. The results presented in this study lay a robust groundwork for future investigations and advancements in the field of highly efficient heterostructure material. These findings have significant implications for the development of environmental remediation strategies and provide valuable insights into sustainable solutions for addressing CPS contamination.

Keywords: Dy₂NdSbO₇; Dy₂NdSbO₇/Bi₂WO₆ heterojunction photocatalyst; chlorpyrifos; visible light irradiation; photocatalytic activity; degradation pathway; degradation mechanism



Citation: Luan, J.; Hao, L.; Yao, Y.; Wang, Y.; Yang, G.; Li, J. Synthesis, Characterization of Dy₂NdSbO₇/Bi₂WO₆ Heterojunction Photocatalyst and the Application for the Photocatalytic Degradation of Chlorpyrifos under Visible Light Irradiation. *Crystals* **2024**, *14*, 55. <https://doi.org/10.3390/cryst14010055>

Academic Editors: Siaw Foon Lee, Chin Wei Lai and Tien-Chien Jen

Received: 29 October 2023

Revised: 27 December 2023

Accepted: 29 December 2023

Published: 30 December 2023



Copyright: © 2023 by the authors. Licensee MDPI, Basel, Switzerland. This article is an open access article distributed under the terms and conditions of the Creative Commons Attribution (CC BY) license (<https://creativecommons.org/licenses/by/4.0/>).

1. Introduction

In order to address the issue of food scarcity caused by population growth, pesticides have been extensively employed in agricultural production to ensure crop yield [1–4]. Among various pesticides, organophosphorus pesticides have gained widespread popularity in the agricultural sector owing to their outstanding efficiency and affordability [5–8]. However, the high toxicity and potential long-term residue of pesticides pose serious concerns as they contaminate soil and jeopardize water resources. Therefore, it is imperative to urgently devise efficacious techniques for eliminating pesticide residues from sewage and purifying freshwater resources.

Chlorpyrifos (CPS), one of the organophosphorus pesticides that has gained penetrative attention, has been targeted for removal from water through various approaches, including biodegradation and chemical degradation. Biodegradation relies on the metabolic capabilities of microorganisms to break down organic pollutants; however, it is limited by microbial activity and environmental factors [9–11]. Chemical degradation, on the other hand, involves chemical reactions to disintegrate organic pollutants. Nonetheless, this method often requires high doses of oxidants or specific pH conditions, which will lead to potential secondary pollution [12–15]. Alternative approaches, including adsorption, ultrasound, coagulation, precipitation, and atmospheric air-cooling plasma, have also been investigated for the removal of CPS. However, these methods tend to be either inefficient, resulting in increased treatment expenses, or result in supplementary contaminants that require additional processing [16–19]. Considering all the above reasons, these methods cannot be directly applied to the actual water pollution control projects.

To overcome these challenges, researchers have been actively seeking highly efficient and environmentally friendly methods to degrade CPS in pesticide wastewater [20–22]. In recent years, photocatalysis technology has garnered significant attention due to its economy, mild reaction conditions, renewability, and versatility [23–25]. The catalyst surfaces could be activated by utilizing light energy, and then photocatalysts can generate highly reactive free radicals capable of rapidly degrading organic pollutants without producing toxic intermediates [26–28]. Therefore, the development of an ideal photocatalyst featuring efficient decoupling of photogenerated charge carriers (PCC), long cycle life and stability, selectivity and controllability, as well as environmental friendliness and sustainability is crucial for the advancement of the water pollution treatment industry.

However, conventional commercial metal oxide photocatalytic nanomaterial, such as TiO_2 and ZnO [29–32], could be stimulated solely by ultraviolet or near-ultraviolet radiation, which constitutes merely 4% of the solar spectrum [33–37]. To fully exploit the segment of visible light ($\lambda > 380 \text{ nm}$), which constitutes the majority of solar energy, the construction of composite materials has emerged as a promising solution. Previous research has demonstrated the excellent photocatalytic performance of AB_2O_6 and $\text{A}_2\text{B}_2\text{O}_7$ compounds under visible light exposure [38–40]. For instance, Devi et al. demonstrated that under visible light exposure for 180 min, the YGdTi_2O_7 nanophase material achieved a photocatalytic removal efficiency (RME) of 66% for methylene blue [41]. Similarly, Zhang et al. studied that the $\text{La}_2\text{Ce}_2\text{O}_7$ photocatalyst powder achieved an RME of 76.6% for methyl orange under visible light exposure for 300 min [42]. Apart from that, Bi_2WO_6 , as an exemplary visible light-driven photocatalytic nanophase material among AB_2O_6 mixtures, has shown remarkable effectiveness in the photodegradation procedure (PDP) of numerous hazardous organic pollutants [43–46]. Furthermore, it is noteworthy that Bi_2WO_6 maintained its crystal structure in the β -pyrochlore-type with an orthorhombic crystal system, belonging to the space group $\text{Pca}2_1$. This structural stability proved to be crucial in ensuring the sustained performance of Bi_2WO_6 during the PDP. Zhao et al. achieved a 70.18% RME of ceftriaxone sodium using Bi_2WO_6 nanoflowers under visible light exposure for 240 min and Lai et al. achieved a 74% RME of erichrome black T using Bi_2WO_6 under exposure for 180 min [47,48]. With a foundation of these promising findings, we have integrated Bi_2WO_6 with our latest research to develop a novel photocatalytic nanophase material that exhibits enhanced performance for water pollution treatment. Further details will be elaborated on in the following parts.

In our previous study, we investigated the potential structural modifications of $\text{Bi}_2\text{InNbO}_7$, a visible light-responsive photocatalyst with a stable pyrochlore structure [49]. By substituting specific elements, we hypothesized that the newly designed $\text{Dy}_2\text{NdSbO}_7$ photocatalyst would exhibit enhanced photocatalytic efficacy by increasing the saturation of PCC.

In the past decade, various strategies have been explored to improve photocatalytic effect, encompassing techniques like surface treatment, doping, and the formation of heterostructures with metals or other semiconductors [50–53]. Among these strategies, the

construction of semiconductor heterojunctions has garnered significant attention due to their remarkable impact on enhancing photocatalytic activity [54–56]. Heterojunction photocatalysts create a potential energy difference at the interface, effectively separating electrons and holes. As a result, the photogenerated carriers can migrate to different active sites, minimizing their recombination rate. This enhanced carrier utilization efficiency contributes to improved photocatalytic performance [57,58]. Additionally, numerous important findings related to semiconductor heterojunction photocatalysts have been documented in recent years. For instance, Xu et al. constructed an AgBr/BiPO₄ heterojunction photocatalyst, which exhibited superior performance in the degradation of Bisphenol S when compared to pure AgBr and BiPO₄ [59]. Wen et al. demonstrated that an AgI/Bi₄V₂O₁₁ heterojunction photocatalyst achieved a higher photodegradation rate for sulfamethazine compared to single catalysts [60].

Based on these fundamental insights, we developed a novel heterostructure photocatalytic material, Dy₂NdSbO₇/Bi₂WO₆, to effectively eliminate CPS from pesticide wastewater under visible light exposure. The experimental results exhibited that the Dy₂NdSbO₇/Bi₂WO₆ heterojunction photocatalyst (DBHP) magnificently included all the dominants of Dy₂NdSbO₇ and Bi₂WO₆, which remained with pyrochlore-type and β-pyrochlore-type structure, respectively. During the PDP, DBHP showcased first-class structural stability and circularity. This result was vigorously demonstrated during the course of the PDP because after 155 min of visible light exposure, DBHP achieved a remarkable CPS removal efficiency of 100%. This further emphasizes its outstanding effectiveness compared to TiO₂ nanoparticles (less than 80% RME) and Cu-ZnO nanocomposite film (less than 81% RME) under identical experimental conditions [61,62]. Additionally, 2.5% decreases in the RME of CPS and TOC were observed in the three consecutive degradation cycles, indicating the structural stability and good reusability of DBHP as a photocatalyst.

In this investigation, comprehensive characterization techniques such as X-ray diffractometer (XRD), Fourier transform infrared (FTIR) spectroscopy, Raman spectroscopy, X-ray photoelectron spectroscopy (XPS), transmission electron microscopy (TEM), and energy dispersive X-ray spectroscopy (EDS) were applied for analyzing the thetastructures of pure phase Dy₂NdSbO₇ and single-phase Bi₂WO₆. Furthermore, the photocatalytic efficacy of CPS in pesticide wastewater under visible light exposure was evaluated for various nanophase materials, including DBHP, Dy₂NdSbO₇, Bi₂WO₆, and nitrogen-doped titanium dioxide. Our study presents a significant innovation by achieving the first-ever synthesis of unprecedented sensitive-to-visible light Dy₂NdSbO₇ nanophase materials with excellent photocatalytic properties using the hydrothermal synthesis technique. This accomplishment represents noteworthy progress in the advancement of an environmentally friendly and efficient photocatalytic system for the degradation of CPS in pesticide wastewater.

2. Experimental Section

2.1. Materials and Reagents

Dy(NO₃)₃·6H₂O (purity = 99.99%), Nd(NO₃)₃·6H₂O (purity = 99.9%), SbCl₅ (purity = 99.99%), Bi(NO₃)₃·5H₂O (purity = 99.99%), and WCl₆ (purity = 99.9%) were purchased from Aladdin Group Chemical Reagent Co., Ltd. (Shanghai, China). Ethylenediaminetetraacetic acid (EDTA, C₁₀H₁₆N₂O₈, purity = 99.5%), isopropyl alcohol (IPA, C₃H₈O, purity ≥ 99.7%), and P-benzoquinone (BQ, C₆H₄O₂, purity ≥ 98.0%) were acquired from Sinopharm Group Chemical Reagent Co., Ltd. (Shanghai, China). Pure ethanol (C₂H₅OH, purity ≥ 99.5%) and CPS (C₈H₁₀NO₅PS, purity ≥ 99.0%) were of gas chromatography grade and met the specifications set by the American Chemical Society, sourced from Aladdin Group Chemical Reagent Co., Ltd. (Shanghai, China).

2.2. Preparation Method of Bi₂WO₆

The Bi₂WO₆ catalyst was fabricated via the hydrothermal method in this study. Following thorough mixing, a precursor solution of the same volume of Bi(NO₃)₃·5H₂O (2 mol/L) and WCl₆ (1 mol/L) was transferred into a polytetrafluoroethylene-lined stain-

less steel autoclave. The reaction medium utilized was a solution composed of glycerol and water, employing polyethylene glycol or ethylene glycol as the dispersant. The solution volume occupied 60% of the autoclave volume. The autoclave was then placed inside a high-temperature sintering furnace and heated to 280 °C under a pressure of 150 MPa. The reaction was allowed to proceed for 1320 min, followed by cooling to room temperature. The resulting mixture underwent centrifugal filtration, followed by washing with acetone, deionized water, and pure ethanol. Subsequently, the material was dried at room temperature under vacuum conditions. The obtained powder mixture was then compressed into thin laminae and sintered in a furnace. The heating profile involved a temperature ramp from 20 °C to 950 °C over 110 min, followed by a 700-min holding period at 950 °C. After the cooling process, the powder pellets were crushed to obtain the desired pure Bi₂WO₆ material.

2.3. Preparation Method of Dy₂NdSbO₇

The Dy₂NdSbO₇ catalyst was prepared via the hydrothermal method in this study. The precursor solutions, including the same volume of Dy(NO₃)₃·6H₂O (2 mol/L), Nd(NO₃)₃·6H₂O (1 mol/L), and SbCl₅ (1 mol/L), were thoroughly mixed. The resulting mixture was then transferred into a polytetrafluoroethylene-lined stainless steel autoclave. A reaction medium composed of a glycerol–water mixture was utilized, while polyethylene glycol or ethylene glycol acted as a dispersant. The solution filled approximately 60% of the autoclave volume. Subsequently, the autoclave was placed into a high-temperature sintering furnace and heated to 240 °C under a pressure of 120 MPa. The reaction was held for 1200 min before cooling to room temperature. The resulting mixture underwent centrifugal filtration, followed by washing steps involving acetone, deionized water, and pure ethanol. The material was then dried under vacuum at room temperature. The obtained powder mixture was pressed into laminae and sintered in a furnace using a heating profile that involved ramping the temperature from 20 °C to 900 °C over 100 min, followed by a 600-min holding period at 900 °C. After cooling, the powder pellets were crushed to obtain the desired pure Dy₂NdSbO₇ material.

2.4. Synthesis of N-Doped TiO₂

The sol–gel synthesis process was applied to fabricate the N-doped TiO₂ (N-dT). The precursor used in this study was tetrabutyl titanate, while ethanol was employed as the solvent. A solution denoted as α was prepared by mixing 35 mL tetrabutyl titanate with 80 mL of absolute ethyl alcohol. Furthermore, solution β was prepared by combining 80 mL of absolute ethyl alcohol with 20 mL of glacial acetic acid and 10 mL of double distilled water. The translucent gel-like suspension was obtained by adding solution α into solution β with the condition of magnetic stirring. Meanwhile, aqua ammonia was employed to immit nitrogen for the aim of achieving an N/Ti proportion of 8 mol%, with the condition of stirring for 60 min. After aging for 48 h, a dry xerogel was formed. The xerogel was then ground and calcined at 400 degrees for 3 h. Finally, the vibrating screen was utilized to obtain the N-dT resulting materials, which served as the nitrogen-doped titania catalyst for subsequent investigations.

2.5. Synthesis of Dy₂NdSbO₇/Bi₂WO₆ Heterojunction Photocatalyst

DBHP was prepared by the solvent-thermal method. First, a precursor solution containing the same volume of Dy(NO₃)₃·6H₂O with a saturation of 2 mol/L, Nd(NO₃)₃·6H₂O with a saturation of 1 mol/L and SbCl₅ with a saturation of 1 mol/L was mixed and stirred for 20 h. The resulting precursor mixture was then transferred into a polytetrafluoroethylene autoclave and maintained at 200 °C for 15 h. Subsequently, under an N₂ atmosphere, the obtained powder was heated in a tubular furnace at a ramping rate of 7.8 °C/min up to 780 °C and held for 8 h for calcination. Finally, pure Dy₂NdSbO₇ powder was obtained.

Next, a precursor solution consisting of the same volume of Bi(NO₃)₃·5H₂O with a saturation of 2 mol/L and WCl₆ with a saturation of 1 mol/L was mixed and stirred for

20 h. The resulting solution was transferred into a polytetrafluoroethylene autoclave and heated at 220 °C for 14 h. Subsequently, under an N₂ atmosphere, the obtained powder was calcined in a tube furnace at a ramping rate of 7 °C/min up to 700 °C for 10 h to obtain pure Bi₂WO₆ powder.

Finally, Dy₂NdSbO₇ powder and Bi₂WO₆ powder, both measured at 1 mol, were mixed in 300 mL octanol (C₈H₁₈O) and sonicated for 1 h in an ultrasonic bath. The mixture was then heated to 150 °C under vigorous stirring conditions and maintained at this temperature for 2 h to facilitate the formation of Dy₂NdSbO₇/Bi₂WO₆ heterojunction photocatalytic material, with Bi₂WO₆ adhering to the surface of Dy₂NdSbO₇ nanoparticles. After cooling to room temperature, the product was obtained by centrifugation and washed multiple times with a mixture of n-hexane and ethanol. The purified powder was dried in a vacuum oven at 60 °C for 6 h and stored in a desiccator for further use. As a result, the Dy₂NdSbO₇/Bi₂WO₆ heterojunction photocatalytic material was successfully prepared.

2.6. Characterization

The pure-phase Dy₂NdSbO₇ and pure-phase Bi₂WO₆ samples, which were fabricated smoothly using the hydrothermal synthesis technique, have been characterized by a set of advanced analytical techniques. For instance, X-ray diffractometer (XRD), transmission electron microscope (TEM), X-ray photoelectron spectrograph (XPS), Fourier Transform Infrared Spectrometer (FTIR), Raman Spectrometer, Inductively Coupled Plasma-Optical Emission Spectrometer (ICP-OES), Fluorescence Spectrophotometer, ultraviolet photoelectron spectroscopy (UPS), and UV-Vis diffuse reflectance spectrophotometer (UV-Vis DRS) were utilized. The X-ray diffractometer (XRD, XRD-6000, Shimadzu Corporation, Kyoto, Japan) was utilized to obtain the XRD analysis. The transmission electron microscope (TEM, Talos F200X G2 TEM, Thermo Fisher Scientific, Waltham, MA, USA) was applied to analyze the morphological and microstructural features of the samples. The UV-Vis diffuse reflectance spectrometer (UV-Vis DRS, UV-3600, Shimadzu Corporation, Kyoto, Japan). The Fourier infrared spectrometer (FTIR, WQF-530A, Beifen-Ruili Analytical Instrument (Group) Co., Ltd., Beijing, China) was employed to analyze the functional groups and chemical bonds. Interactions among various chemical bonds were analyzed using a Raman spectrometer (INVIA0919-06, RENISHAW plx, Wotton-under-Edge, Gloucestershire GL 12 8JR, London, UK). The surface chemical composition and states were examined by an X-ray photoelectron spectrometer (XPS, PHI 5000 VersaProbe, UIVAC-PHI, Maoqi city, Japan) and an Inductively Coupled Plasma-Optical Emission Spectrometer (ICP-OES, PlasmaQuant 9100, Analytik Jena AG, Jena city, Germany). The ionization potential of the valence band of the samples was detected by ultraviolet photo-electron spectroscopy (UPS, Escalab 250 xi, Thermo Fisher Scientific, Waltham, MA, USA).

2.7. Photoelectrochemical Experiments

The electrochemical workstation (CHI660D, Chenhua Instruments Co., Ltd., Shanghai, China) was employed to actualize the electrochemical impedance spectroscopy (EIS) experiment. The three-electrode system consisted of the working electrode, the counter electrode, and the reference electrode. In this setup, the as-prepared catalysts were used as the working electrode, a platinum plate served as the counter electrode, and an Ag/AgCl electrode was utilized as the reference electrode. Lee et al. made a significant and notable contribution to this study by discovering the influence of pH on the OH⁻ / •OH potential and the standard potential of reactive oxygen species [30]. Therefore, the electrolyte used was a 0.5 mol/L Na₂SO₄ hydrous solution at pH 7. A 500 W Xe lamp with a 420 nm cut-off filter was utilized as the light source during the experimental procedure.

2.8. Experimental Setup and Procedure

The photocatalytic reactor (CEL-LB70, China Education Au-Light Technology Co., Ltd., Beijing, China) was applied to actualize degradation experiments. The visible light was simulated by a xenon lamp (500 W) and a cut-off filter (420 nm).

In every trial, a set of 12 quartz tubes with a capacity of 45 mL was used for individual reaction solutions. For chemical industry wastewater, the overall reaction volume was 540 mL. The nanophase materials dosage for each experiment ($\text{Dy}_2\text{NdSbO}_7$, Bi_2WO_6 or DBHP) was maintained at 0.5 g/L. The initial saturation of CPS in the solution was 0.025 mmol/L.

During the reaction, a 4 mL aliquot of the dispersed system was periodically sampled for analysis. After 155 min of light exposure, a 5 mL aliquot of the dispersed system was collected to measure the residual CPS saturation. The photocatalyst was subsequently removed by filtration using a 0.22 μm PES polyether sulfone filter membrane. The remaining CPS saturation was determined using Agilent 200 high-performance liquid chromatography (Agilent Technologies, Palo Alto, CA, USA) with a mobile phase composed of 50% CH_3CN and 50% distilled deionized water. The post-PDP of the CPS dispersed system was injected with a volume of 10 μL with the flow rate condition of 1 mL/min.

To establish adsorption/desorption equilibrium between the photocatalytic sample, CPS, and atmospheric oxygen, the dispersed system containing the sample and CPS was magnetically stirred in darkness for 45 min prior to light exposure. During exposure, the dispersed system was stirred at a speed of 500 r.

The TOC analyzer (TOC-5000 A, Shimadzu Corporation, Kyoto, Japan) was utilized to evaluate the mineralization results of CPS in the reaction dispersed system. The TOC saturation during CPS PCP was calibrated using either potassium acid phthalate ($\text{KHC}_8\text{H}_4\text{O}_4$) or anhydrous sodium carbonate as the regulation reactant. Calibration standards were fabricated using potassium acid phthalate with known carbon saturation ranging from 0 to 100 mg/L. TOC saturation was evaluated in six samples with the reaction solution of 45 mL in each specimen.

The liquid chromatography-mass spectrometry (LC-MS, Thermo Quest LCQ Duo, Thermo Fisher Scientific Corporation, Waltham, MA, USA) was applied to calibrate the intermediate reactants during the calibration experiments. The Beta Basic-C18 HPLC column (150 \times 2.1 mm, 5 μm ID, Thermo Fisher Scientific Corporation, Waltham, MA, USA) was applied during the PCP of CPS. A 20 μL solution obtained after the photocatalytic reaction was automatically injected into the LC-MS system. The mobile phase consisted of 60% methanol and 40% ultrapure water, flowing through the system at a rate of 0.2 mL/min. The spray voltage was set at 4500 V, while the capillary temperature and voltage were maintained at 27 $^\circ\text{C}$ and 19.00 V, respectively. The mass-to-charge ratio (m/z) range for analysis was set from 50 to 500.

To assess the photon intensity of the irradiating light, a filter (420 nm) was applied to choose the radiation range in the visible light waverange. The number of photons passing through the filter per unit time, either total photons or reactive photons, can be calculated using the formula $\nu = c/\lambda$. Here, ν represents the frequency of photons, λ corresponds to the wavelength of incident light, and c signifies the speed of light. Based on the unambiguous numerical value of the Avogadro invariable (NA) and Planck invariable (h), the numerical value of energy of a photon ($h\nu$) can be obtained smoothly. The irradiation photon flux can be acquired by adjusting the interspace between the photoreactor and the light source. And the radiometer (Model FZ-A, Photoelectric Instrument Factory Beijing Normal University, Beijing, China) was employed to evaluate the incident photon flux I_0 . The numerical value was determined to be 4.76×10^{-6} Einstein $\text{L}^{-1} \text{s}^{-1}$ under light exposure.

The photonic efficiency (PHE) was determined with Equation (1):

$$\phi = R/I_0 \quad (1)$$

where ϕ is the PHE (%), R is the retrogradation velocity of CPS ($\text{mol L}^{-1} \text{s}^{-1}$), and I_0 is the irradiation photon flux (Einstein $\text{L}^{-1} \text{s}^{-1}$).

3. Result and Discussion

3.1. XRD Analysis

Figure 1 showcases the XRD imageries of DBHP, $\text{Dy}_2\text{NdSbO}_7$, and Bi_2WO_6 . The presence of prominent peaks and crystal planes from both $\text{Dy}_2\text{NdSbO}_7$ and Bi_2WO_6 in the XRD imagery of DBHP corroborates the successful synthesis of DBHP. The obtained data for $\text{Dy}_2\text{NdSbO}_7$ and Bi_2WO_6 compounds were further subjected to Rietveld refinement using the Materials Studio program, as showcased in Figures 2a and 3a, respectively. The refined results for $\text{Dy}_2\text{NdSbO}_7$ ($R_p = 5.45\%$) and Bi_2WO_6 ($R_p = 8.73\%$) exhibit admirable consistency between the experimental and theoretical intensities, confirming the pyrochlore-type structure of $\text{Dy}_2\text{NdSbO}_7$ and β -pyrochlore-type structure of Bi_2WO_6 . Moreover, both compounds are determined to be single-phase, with $\text{Dy}_2\text{NdSbO}_7$ crystallizing in the cuboidal lattice with the space group $Fd3m$, while Bi_2WO_6 crystallizes in the orthorhombic crystal system with the space group $Pca21$. The lattice space constants for $\text{Dy}_2\text{NdSbO}_7$ and Bi_2WO_6 are determined to be $10.499(3) \text{ \AA}$ and $10.819(8) \text{ \AA}$, respectively. The refinement model, which considers the presence of O atoms, showcased admirable consistency between the experimental and theoretical intensities.

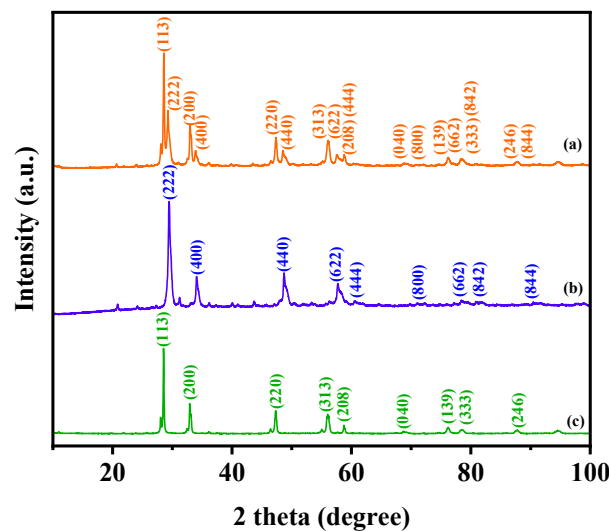


Figure 1. XRD imageries of (a) DBHP, (b) $\text{Dy}_2\text{NdSbO}_7$, and (c) Bi_2WO_6 .

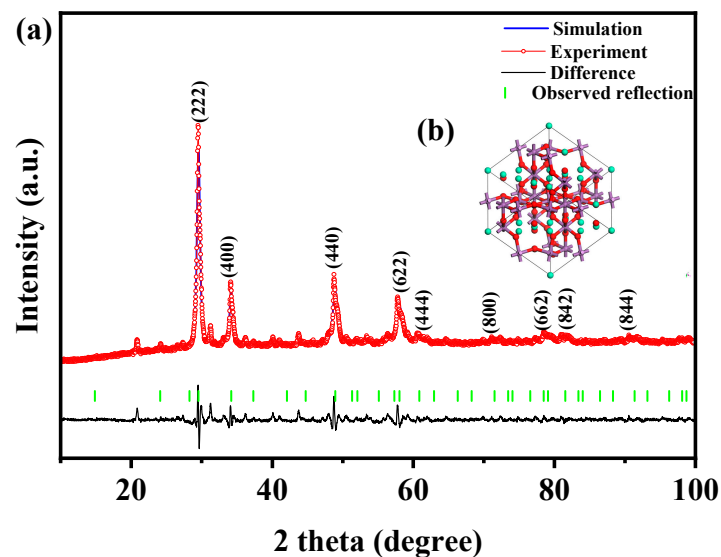


Figure 2. (a) XRD imagery and Rietveld refinement and (b) the atomic structure (red atom: O, purple atom: Nd or Sb, green atom: Dy.) of $\text{Dy}_2\text{NdSbO}_7$.

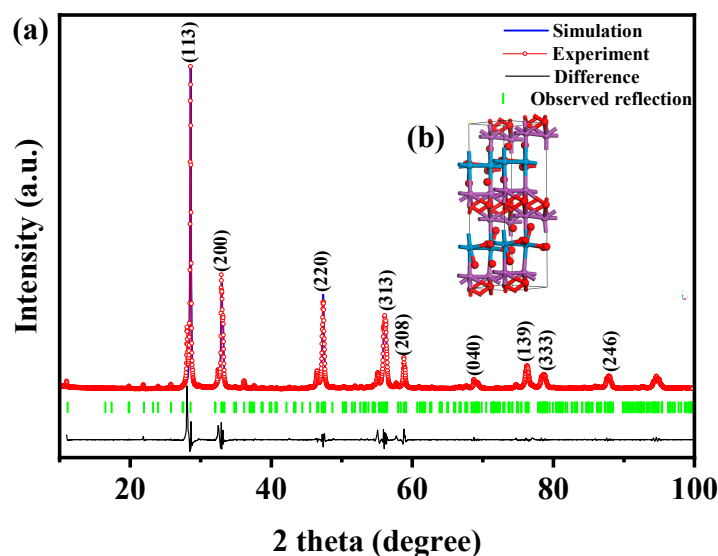


Figure 3. (a) XRD pattern and Rietveld refinement and (b) the atomic structure (red atom: O, blue atom: W, purple atom: Bi.) of Bi_2WO_6 .

The atomic structures of $\text{Dy}_2\text{NdSbO}_7$ and Bi_2WO_6 are showcased in Figures 2b and 3b, respectively. Additionally, Tables 1 and 2 provide the atomic coordinates and structural parameters for $\text{Dy}_2\text{NdSbO}_7$ and Bi_2WO_6 , respectively. These comprehensive analyses demonstrate the excellent structural stability of the synthesized compounds and further highlight their potential applicability as highly efficient photocatalysts in various fields.

Table 1. Structural eigenvalues of $\text{Dy}_2\text{NdSbO}_7$ fabricated by hydrothermal synthesis technique.

Atom	x	y	z	Occupation Factor
Dy	0	0	0	1
Nd	0.5	0.5	0.5	0.5
Sb	0.5	0.5	0.5	0.5
O(1)	−0.168	0.125	0.125	1
O(2)	0.125	0.125	0.125	1

Table 2. Structural eigenvalues of Bi_2WO_6 fabricated by hydrothermal synthesis technique.

Atom	x	y	z	Occupation Factor
Bi(1)	0.0000	0.1386	0.5665	0.64
W(1)	0.0000	0.1386	0.5665	0.36
Bi(2)	0.0000	0.1842	0.2500	0.78
W(2)	0.0000	0.1842	0.2500	0.22
O(1)	0.0000	0.7554	0.25000	1.00
O(2)	0.0000	0.0429	0.1172	1.00
O(3)	0.0000	0.3368	0.0845	1.00

The distortions observed in the MO_6 ($\text{M} = \text{Nd}^{3+}$ and Sb^{5+}) octahedra of $\text{Dy}_2\text{NdSbO}_7$ suggest a crystal structure distortion, which has been certified to reinforce the photocatalytic effect in previous studies [63]. Furthermore, the unique crystal structure of $\text{Dy}_2\text{NdSbO}_7$, with a spatial mesh structure composed of vertices of MO_6 ($\text{M} = \text{Nd}^{3+}$ and Sb^{5+}) octahedra connected by Dy^{3+} ions, exhibits a distinct Dy-O bond connecting distance and bond angles. Specifically, the six Dy-O(1) bonds connecting distance (4.206 Å) are lengthier than the two Sm-O(2) bonds connecting distance (2.687 Å). The M-O-M bond angles are measured at 136.62° , while the Dy-M-Dy bond angles are 120.00° in the crystal structure of $\text{Dy}_2\text{NdSbO}_7$. The angle of the M-O-M bond acts as a decisive factor in determining the delocalization of the stimulated state, and bond angles closer to 180° are known to enhance luminescent

properties [63]. The M-O-M bond angles in Dy₂NdSbO₇ can influence the photocatalytic efficacy by affecting the mobility of PCC, which in turn influences their likelihood of entering the reaction centers on the samples surface. Moreover, the larger Dy-Nd-O and Dy-Sb-O bond angles in Dy₂NdSbO₇ may enhance its photocatalytic properties.

The photocatalytic properties of monocrystalline catalytic materials heavily rely on the size of the crystallites, thereby emphasizing the necessity of precise determination of crystallite size in polycrystalline samples. X-ray powder diffraction, in conjunction with the Scherrer Equation (2), is a prevalent and well-established approach used to accomplish this crucial measurement in scientific research [64–66].

$$D = \frac{K\lambda}{\beta \cos\theta} \quad (2)$$

In the given equation, D represents the coherent diffraction domain size. The wavelength of the Cu target (1.54056 Å) used in the X-ray diffractometer is denoted by λ . The reflection width at 2θ is represented by β and θ denotes the Bragg angle. To ensure dimensional consistency, a shape constant (K) of approximately 0.9 is commonly used, irrespective of the crystal morphology or reflection index. It is important to note that the shape constant should be expressed in radians. Therefore, when employing a value of 0.9 for the shape constant, it is essential to express the reflection width (β) in radians. For Dy₂NdSbO₇, the peak of the (222) crystal plane in the XRD spectrum was located at $2\theta = 29.975^\circ$, with a corresponding FWHM of 0.051 nm. On the other hand, for Bi₂WO₆, the peak of the (113) crystal plane was located at $2\theta = 29.275^\circ$, with an FWHM of 0.042 nm. Subsequently, the monocrystalline sizes of Dy₂NdSbO₇ and Bi₂WO₆ photocatalytic materials were calculated as 391.812 nm and 322.146 nm, respectively. Based on this analysis, it can be concluded that Dy₂NdSbO₇ possesses a larger specific surface area and more reactive sites on its surface compared to Bi₂WO₆.

Consequently, the remarkable performance of Dy₂NdSbO₇ in the photocatalytic degradation of the targeted pollutant can be credited to both its idiographic crystalline nature and electronic thetastructure. These insights into the crystallographic and electronic properties of Dy₂NdSbO₇ are of great significance in understanding and optimizing its photocatalytic capabilities.

3.2. FTIR Analysis

To analyze the functional groups and chemical bonds in DBHP, Dy₂NdSbO₇, and Bi₂WO₆, FTIR spectroscopy was performed using an FTIR spectrometer, as illustrated in Figure 4 [67]. The obtained FTIR spectra exhibited distinct absorption peaks associated with specific bonds, including Dy-O, Nd-O, Sb-O, Sb-O-Sb, Bi-O, W-O, and W-O-W. The stretching oscillation of Dy-O occurred at 430 cm⁻¹, while the bending oscillation of Nd-O was observed at 552 cm⁻¹ [68–70]. The peak at 543 cm⁻¹ indicated the stretching oscillation of Bi-O, and the bending oscillation of Sb-O appeared at 657 cm⁻¹ [71–73]. The bending oscillation of Sb-O-Sb was represented by peaks at 696 cm⁻¹ [74]. Additionally, the stretching oscillation of W-O and W-O-W bonds was detected at 738 cm⁻¹ and 815 cm⁻¹, respectively [75].

Moreover, the stretching oscillation mode of O-H groups derived from chemisorbed water molecules was observed at the broad peak around 3460 cm⁻¹ [76,77]. The bending oscillation of surface OH groups was credited to the absorption peak at 1632 cm⁻¹ [78]. The peak at 1387 cm⁻¹ could be attributed to the symmetric and anti-symmetric modes of the C-H bond [79–81].

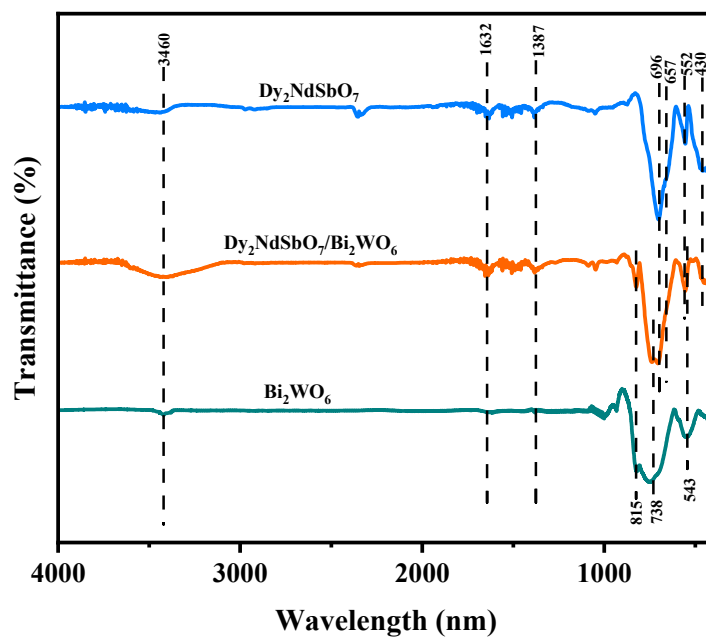


Figure 4. FTIR spectra of $\text{Dy}_2\text{NdSbO}_7$, Bi_2WO_6 , and DBHP.

3.3. Raman Analysis

To analyze the chemical structure, phase and molecular interactions of DBHP, $\text{Dy}_2\text{NdSbO}_7$, and Bi_2WO_6 , Raman spectroscopy was performed using a spectrometer to examine the chemical bond interactions in DBHP, $\text{Dy}_2\text{NdSbO}_7$, and Bi_2WO_6 . Figure 5a–c present the Raman spectra obtained for $\text{Dy}_2\text{NdSbO}_7$, Bi_2WO_6 , and DBHP. In $\text{Dy}_2\text{NdSbO}_7$, characteristic modes were observed, including B_{1g} anti-symmetric modes of the Sb–O bond and Dy–O bond at 639 cm^{-1} and 708 cm^{-1} , respectively [82–85]. Additionally, the Nd–O bond exhibited an A_{1g} bending vibration mode at 803 cm^{-1} [86]. The Raman spectra of Bi_2WO_6 exhibited characteristic modes such as the A_g internal stretching mode of Bi–O at 149 cm^{-1} , and E_{1g} vibrational modes at 282 cm^{-1} , 305 cm^{-1} , and 333 cm^{-1} arising from the stretching of W–O bonds. Peaks at 715 cm^{-1} , 793 cm^{-1} , and 831 cm^{-1} corresponded to the anti-symmetric and symmetric A_g modes of terminal O–W–O groups [87,88]. These observed peaks confirmed the presence of pure phases, consistent with XRD results. The Raman spectrum of DBHP exhibited distinctive peaks at 149 cm^{-1} , 282 cm^{-1} , 305 cm^{-1} , 333 cm^{-1} , 639 cm^{-1} , 720 cm^{-1} , 792 cm^{-1} , and 831 cm^{-1} , which were indicative of the characteristic features of both $\text{Dy}_2\text{NdSbO}_7$ and Bi_2WO_6 . Additionally, the deconvolution spectra of the peaks at 720 cm^{-1} and 792 cm^{-1} in the Raman spectrum of DBHP are showcased in Figure 5d,e, respectively. The fitted peaks were consistent with the corresponding peaks in the Raman spectra of $\text{Dy}_2\text{NdSbO}_7$ and Bi_2WO_6 . Due to all characteristic peaks of individual $\text{Dy}_2\text{NdSbO}_7$ and Bi_2WO_6 , photocatalytic materials can be indexed in the Raman spectrum of DBHP; therefore, the heterostructure was fabricated ideally within DBHP. These results further supported the successful integration of both materials within the heterojunction photocatalyst.

3.4. UV-Vis Diffuse Reflectance Spectra

To investigate the band structure of the synthesized samples, the absorption spectra of $\text{Dy}_2\text{NdSbO}_7$, Bi_2WO_6 , and DBHP are analyzed and presented in Figure 6a. The absorption spectrum verge of $\text{Dy}_2\text{NdSbO}_7$ and Bi_2WO_6 were observed at 456 nm and 477 nm , respectively. Notably, the absorption spectrum verge of DBHP was positioned in 500 nm , indicating a palpable red-shift in comparison with Bi_2WO_6 and $\text{Dy}_2\text{NdSbO}_7$. This finding suggests that DBHP exhibits a higher light absorption capacity than Bi_2WO_6 and $\text{Dy}_2\text{NdSbO}_7$.

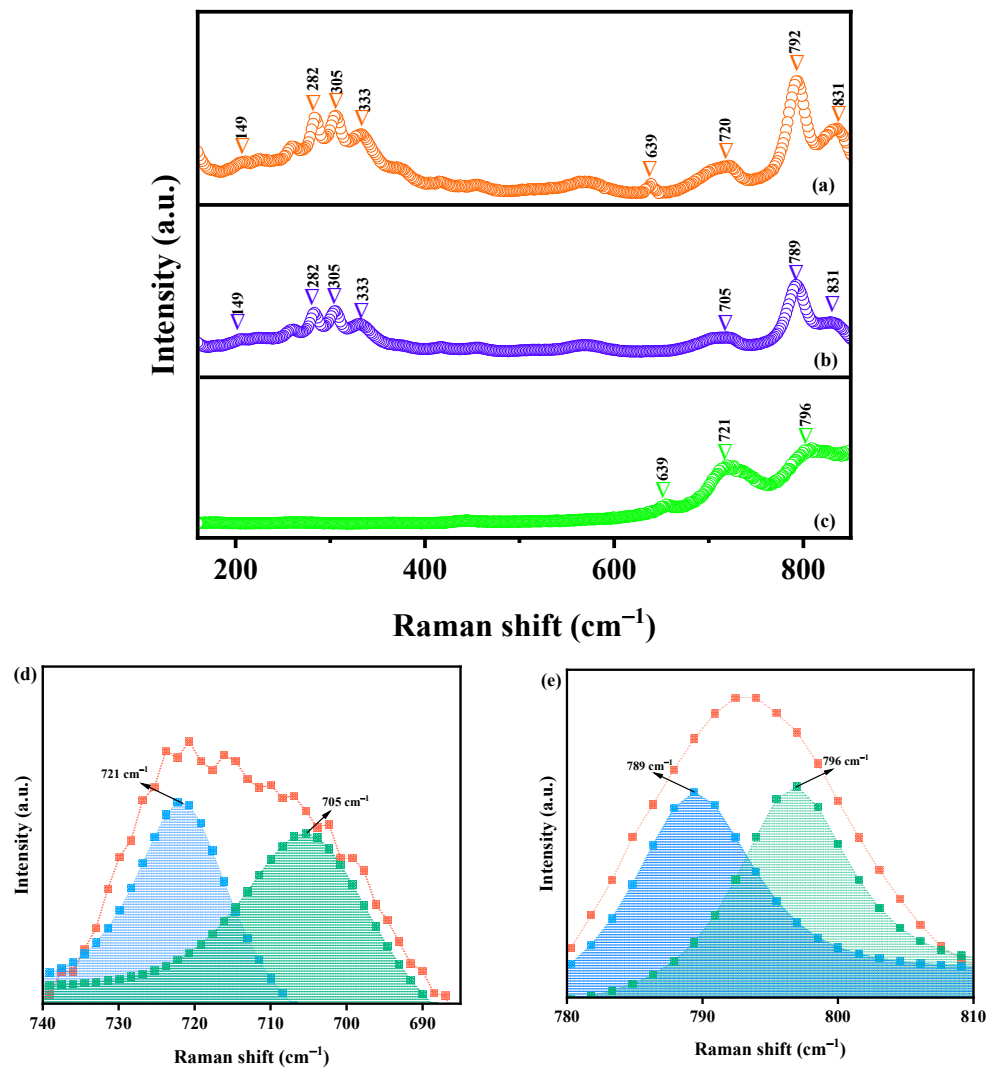


Figure 5. Raman spectra of (a) DBHP, (b) Bi_2WO_6 , and (c) $\text{Dy}_2\text{NdSbO}_7$, and deconvolution spectra of peaks at (d) 720 cm^{-1} and (e) 792 cm^{-1} in the Raman spectrum of DBHP.

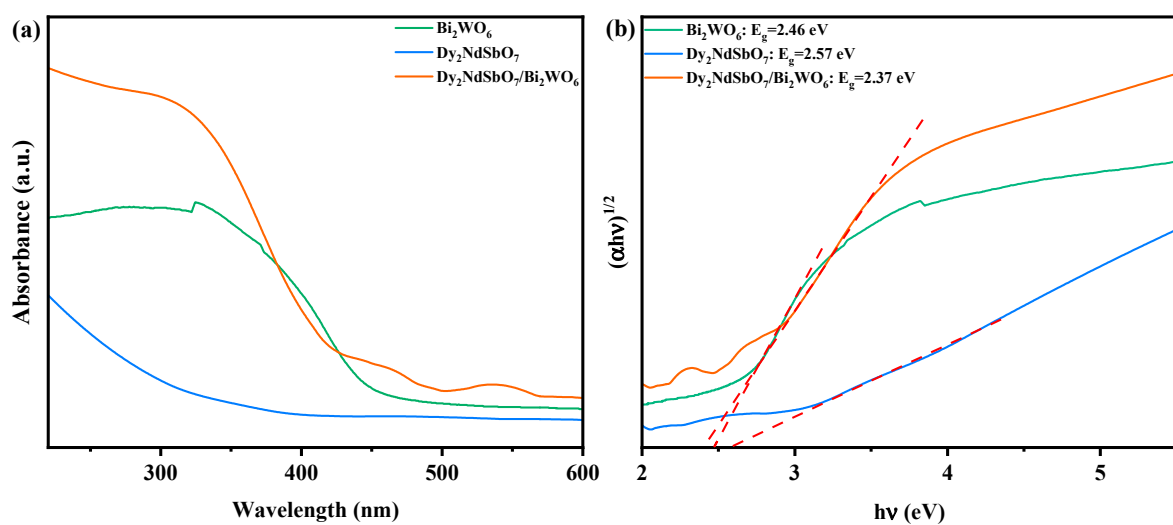


Figure 6. (a) The UV-Vis diffuse reflectance spectra and (b) correlative diagram of $(\alpha hv)^{1/2}$ and hv of the synthesized DBHP, $\text{Dy}_2\text{NdSbO}_7$, and Bi_2WO_6 (red dash lines: the linear fit of the correlative diagram).

The energy difference between bands in samples can be achieved by identifying the crossing point at which the photon energy ($h\nu$) axis intersects the line extrapolated from the linear part of the absorption spectrum verges, known as the Kubelka–Munk function (3) [89,90].

$$\frac{[1 - R_d(h\nu)]^2}{2R_d(h\nu)} = \frac{\alpha(h\nu)}{S} \quad (3)$$

In this mathematical equation, the scattering eigenvalues, the diffuse reflection modulus, or the radiation absorption modulus were assigned to S , R_d , or α , respectively.

The optical absorption characteristics close with the band verges of the samples cohered with Equation (4) [91,92]:

$$(\alpha h\nu)^{\frac{1}{n}} = A(h\nu - E_g) \quad (4)$$

In this mathematical equation, the proportional invariable, absorption modulus, band gap, or light frequency were assigned to A , α , E_g , or ν , respectively. The numerical value of n masters the transition property of photocatalytic samples. The numerical value of the n modulus is determined by the characteristics of electronic transitions. Specifically, for direct bandgap transitions, the n value is equal to $1/2$, while for indirect bandgap transitions, the n value is equal to 2 [93].

According to the findings in Figure 6b, the calculated E_g values for $\text{Dy}_2\text{NdSbO}_7$ and Bi_2WO_6 were 2.57 eV and 2.42 eV, respectively. The values of E_g were the intersections of the linear fit (red dash lines) and the x-axis in Figure 6b [94]. The numerical value of n was approximately 2 for both $\text{Dy}_2\text{NdSbO}_7$ and Bi_2WO_6 , indicating that the photic transitions were indirectly allowed [94]. By similar analysis grounded on Figure 6b, the E_g numerical value for DBHP was determined to be 2.37 eV, also indicating an indirectly allowed optical transition.

3.5. X-ray Photoelectron Spectroscopy Analysis

The X-ray photoelectron spectroscopy (XPS) was applied to evaluate the chemical composition and oxidation states of DBHP, $\text{Dy}_2\text{NdSbO}_7$, and Bi_2WO_6 [95]. The survey spectrum in Figure 7 revealed the presence of Dy, Nd, Sb, Bi, W, and O elements in DBHP. A carbon peak, attributed to adventitious hydrocarbon, served as a calibration reference. Furthermore, comparing the spectrum of $\text{Dy}_2\text{NdSbO}_7$ with DBHP, clear Bismuth and Tungsten signals were observed in the latter, indicating the inclusion of Bi_2WO_6 in DBHP.

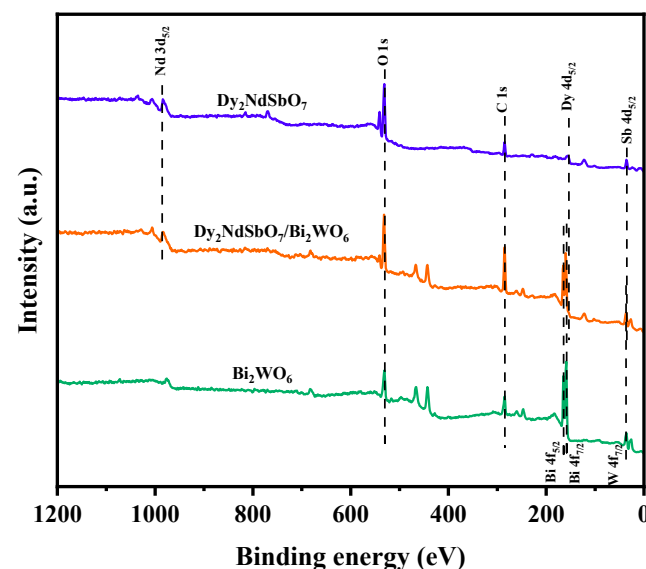


Figure 7. The XPS full spectrum of the synthesized DBHP, $\text{Dy}_2\text{NdSbO}_7$, and Bi_2WO_6 .

Figure 8a–c displayed the spectral peaks of Dy 4d, Nd 3d, and Bi 4f in Dy₂NdSbO₇, Bi₂WO₆, and DBHP. These peaks were observed at 154.78 eV (Dy 4d_{5/2}), 983.23 eV (Nd 3d_{5/2}), 159.19 eV (Bi 4f_{7/2}), and 164.35 eV (Bi 4f_{5/2}) in the two compounds. Notably, these peaks exhibited slight shifts towards higher binding energies in DBHP, such as 154.41 eV (Dy 4d_{5/2}), 983.49 eV (Nd 3d_{5/2}), 159.19 eV (Bi 4f_{7/2}), and 164.85 eV (Bi 4f_{5/2}). The observed shifts provided strong evidence of a notable interfacial interaction between Dy₂NdSbO₇ and Bi₂WO₆, which could potentially be credited to electron conduction and delocalization phenomena occurring between both components. Additionally, Figure 8d presented the peak deconvolution spectrum of Sb 4d and W 4f in DBHP, corresponding to peaks in Dy₂NdSbO₇ and Bi₂WO₆. The peaks at 34.87 eV (W 4f_{7/2}), 35.53 eV (Sb 4d_{5/2}), and 37.23 eV (W 4f_{5/2}) exhibited slight up-shifts in binding energies, measuring 35.37 eV (W 4f_{7/2}), 35.79 eV (Sb 4d_{5/2}), and 37.73 eV (W 4f_{5/2}) in DBHP, respectively [96]. Moreover, the spin-orbit separation values between Bi 4f_{7/2} and Bi 4f_{5/2} were 5.16 eV for both Bi₂WO₆ and DBHP, indicating the exclusive presence of Bi³⁺ [97]. Similarly, the spin-orbit separation values between W 4f_{7/2} and W 4f_{5/2} were 2.36 eV for both Bi₂WO₆ and DBHP, indicating the exclusive presence of W⁶⁺.

Figure 8e showcases the deconvoluted O 1s spectrum of DBHP, Dy₂NdSbO₇, and Bi₂WO₆. The observed peaks at 529.9 eV, 529.64 eV, and 529.4 eV correspond to the lattice oxygen [98]. Furthermore, the peaks at 530.97 eV, 529.71 eV, and 529.47 eV signify the signal originating from hydroxyl groups [99]. Additionally, the peaks at 531.6 eV, 531.34 eV, and 531.1 eV correspond to the signal associated with oxygen vacancies [98,99]. Notably, in the case of DBHP, the location of the deconvoluted O 1s peaks manifested evident shifts in comparison to their positions in pure Dy₂NdSbO₇ and Bi₂WO₆ samples. These shifts provided further evidence of interfacial interactions between Dy₂NdSbO₇ and Bi₂WO₆ species. Moreover, the spin-orbit disassociation numerical value between Sb 3d_{5/2} and Sb 3d_{3/2} was consistently measured as 8.75 eV for both Dy₂NdSbO₇ and DBHP, which confirms the exclusive presence of Sb⁵⁺ species [100].

Based on the XPS analysis, it is concluded that the oxidation states of Dy, Nd, Sb, Bi, W, and O ions in the material are +3, +3, +5, +3, +6, and −2, respectively. Moreover, the surface elemental analysis revealed an average atomic ratio of Dy:Nd:Sb:Bi:W:O as 870:427:427:891:443:6942, indicating the atomic ratios of Dy:Nd:Sb and Bi:W in the DBHP sample of 2.04:1.00:1.00 and 2.01:1.00, respectively. No additional phases were observed by analyzing the XPS peaks of Dy₂NdSbO₇ and Bi₂WO₆, confirming their absence.

The transmission electron microscopy (TEM) and energy-dispersive X-ray spectroscopy (EDS) were applied to investigate the thetastructure and elemental composition of DBHP [101]. TEM image, HRTEM image, and EDS mapping (Figures 9 and 10) clearly indicated that the biggish particles corresponded to Dy₂NdSbO₇, while the minor circular-shaped microparticles belonged to Bi₂WO₆. This observation provided strong evidence confirming the successful synthesis of DBHP, with Dy₂NdSbO₇ particles visibly surrounded by Bi₂WO₆ microparticles. The microparticle sizes were measured to be approximately 310 nm for Bi₂WO₆ and 400 nm for Dy₂NdSbO₇. The measured microparticle sizes were close to the accurate numerical value calculated by the Scherrer equation in the XRD analysis part. Furthermore, the high-resolution TEM micrograph (HRTEM) depicted in Figure 9b reveals interplanar crystal spacing *d* numerical value of 0.909 nm and 0.326 nm, corresponding to the (222) crystallographic plane of Dy₂NdSbO₇ and the (113) crystallographic plane of Bi₂WO₆, respectively. And the tight interfacial contact between the two samples in the heterojunction was also emphasized. This unequivocally confirms the coexistence of both Dy₂NdSbO₇ and Bi₂WO₆ in the fabricated heterojunction.

The EDS element mapping analysis (Figure 10) further confirmed the presence of dysprosium, neodymium, stibium, bismuth, tungsten, and oxygen elements within DBHP, providing strong support for the coexistence of Dy₂NdSbO₇ and Bi₂WO₆. These findings corresponded to the XPS upshots depicted in Figures 7 and 8. Additionally, the EDS spectrum (Figure 11) revealed an atomic ratio of approximately 873:424:429:892:438:6944 for Dy:Nd:Sb:Bi:W:O in DBHP, which matched well with the XPS results. The calculated

atomic ratio between $\text{Dy}_2\text{NdSbO}_7$ and Bi_2WO_6 was approximately 1.3:1, corresponding to the approximate molar ratio used during the synthesis. Based on these comprehensive results, it can be convincingly concluded that DBHP was successfully synthesized with high purity under the employed preparation conditions.

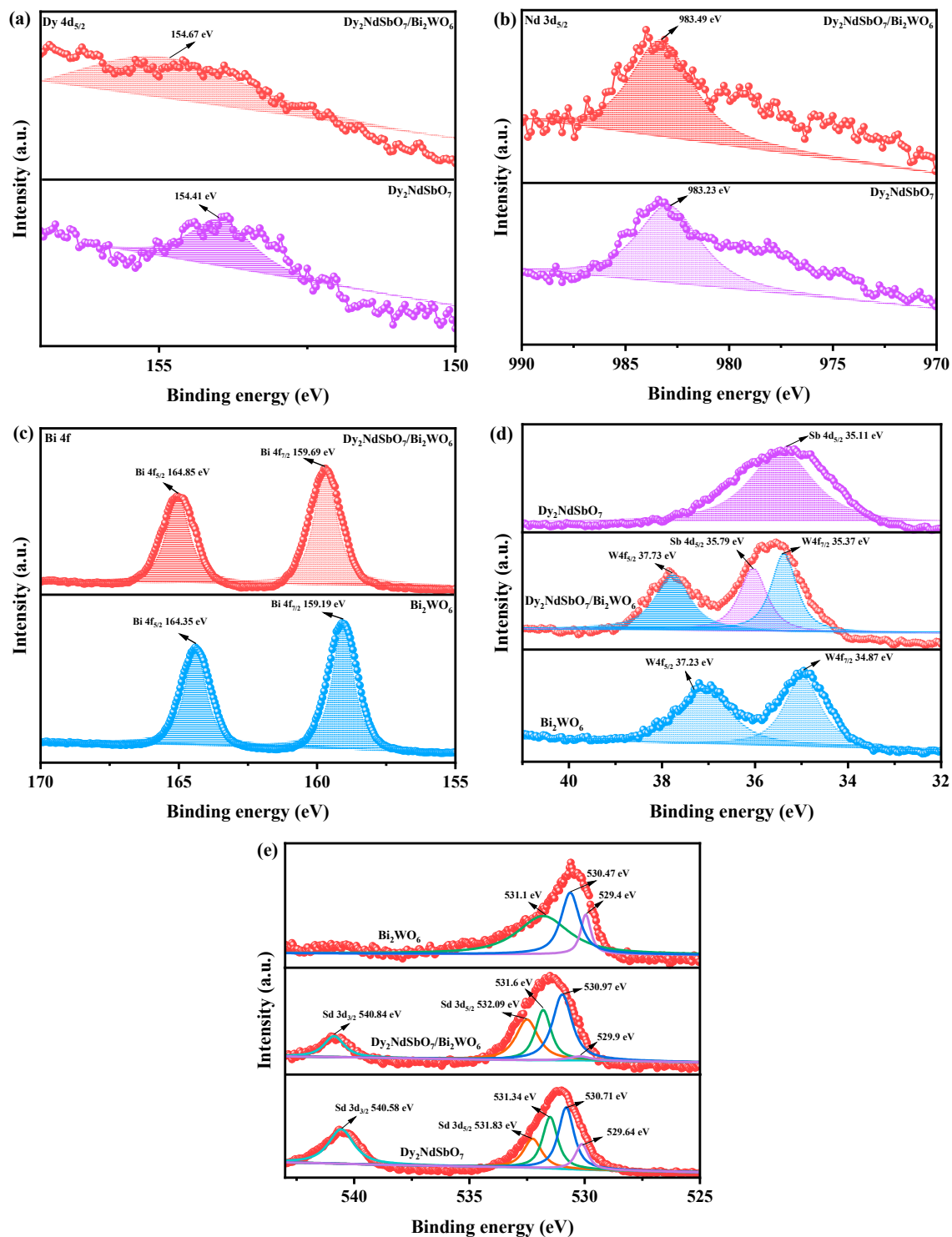


Figure 8. The corresponding high-resolution XPS spectra of (a) Dy 4d, (b) Nd 3d, (c) Bi 4f, (d) Sb 4d and W 4f, (e) O 1s, and Sb 3d of DBHP, $\text{Dy}_2\text{NdSbO}_7$, and Bi_2WO_6 (the black arrows indicated the position of the spectral peaks).

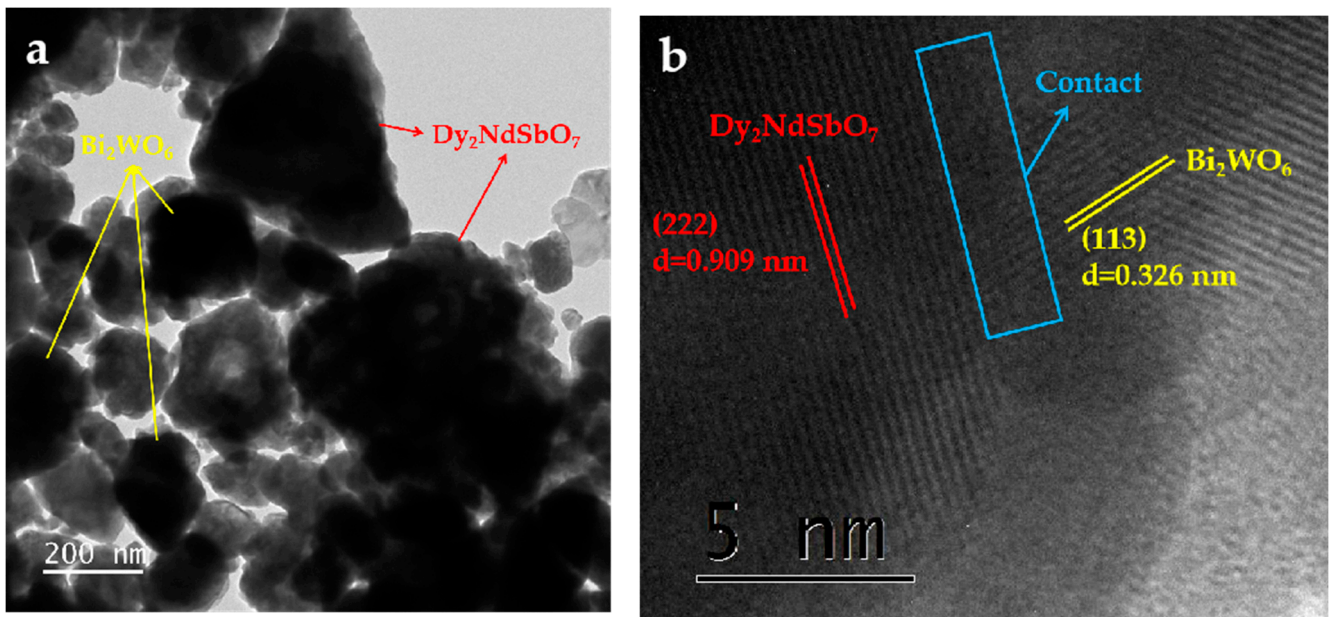


Figure 9. (a) TEM image and (b) HRTEM image of DBHP.

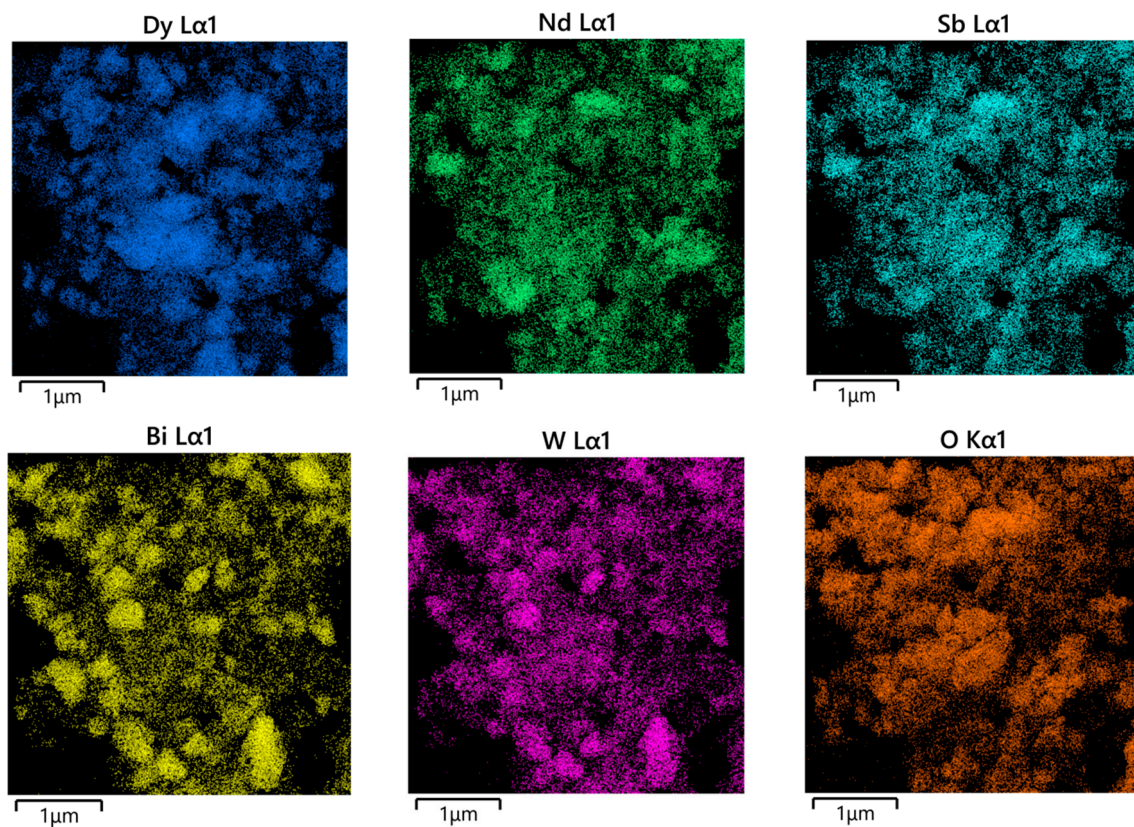


Figure 10. EDS elemental mapping of DBHP (Dy, Nd, Sb, O from $\text{Dy}_2\text{NdSbO}_7$ and Bi, W, O from Bi_2WO_6).

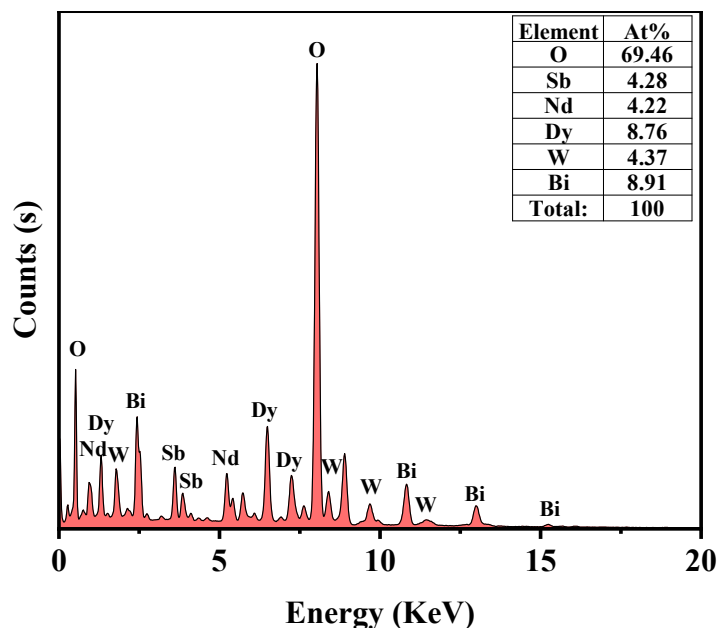


Figure 11. The EDS spectrum of DBHP.

Additionally, ICP-OES analysis for DBHP is showcased in Table 3 [102–104]. The experimental molar ratios of DBHP were found to closely match the numerical value in the XPS part and EDS part. And the molar ratios obtained from ICP-OES analysis indicated a ratio of 2.02:1.02:1.00:2.03:1.00, which closely approximated the theoretical ratio of 2:1:1:2:1. Moreover, the ICP-OES analysis validated the accuracy of the photocatalyst preparation process. The close compatibility between the experimental and theoretical molar ratios of the metal elements suggests the successful fabrication of the heterostructure photocatalyst.

Table 3. ICP-OES analysis for DBHP.

Photocatalyst	ICP-OES Results (mg/Kg)	mol/Kg	Theoretical Mole Ratio (Dy:Nd:Sb:Bi:W)	Experimental Mole Ratio (Dy:Nd:Sb:Bi:W)
Dy ₂ NdSbO ₇ /Bi ₂ WO ₆	Dy = 142,378.60	0.89	2:1:1:2:1	2.03:1.02:1.00:2.03:1.00
	Nd = 64,890.11	0.45		
	Sb = 53,160.15	0.44		
	Bi = 185,742.25	0.89		
	W = 80,642.25	0.44		

3.6. Photocatalytic Activity

3.6.1. Photocatalytic Activity in Photodegradation Experiments

The photocatalytic efficacy of the N-dT, Dy₂NdSbO₇, Bi₂WO₆, and DBHP were compared in terms of the ability to degrade CPS ($C_{\text{CPS}} = 0.025$ mmol/L, $C_{\text{photocatalyst}} = 0.5$ g/L). N-dT, which was recognized as a widely accepted visible-light responsive photocatalyst, was used as a benchmark photocatalyst to compare the photocatalytic effect differences among various samples. Figure 12a–d illustrate the UV-Vis absorption spectra of the CPS dispersed system at various degradation times using N-dT, Dy₂NdSbO₇, Bi₂WO₆, and DBHP as a photocatalyst, respectively. The residual saturation of CPS was determined grounded on the absorbance of the CPS saturation at its maximum absorption wavelength (~610 nm) during the PDP. It is evident that the coupling of Dy₂NdSbO₇ and Bi₂WO₆ confers superior photocatalytic efficacy to the derived DBHP compared to individual Dy₂NdSbO₇ and Bi₂WO₆. This observation suggested that the formation of a heterojunction in the DBHP promotes the efficient disassociation of PCC, thereby synergistically enhancing the PDP.

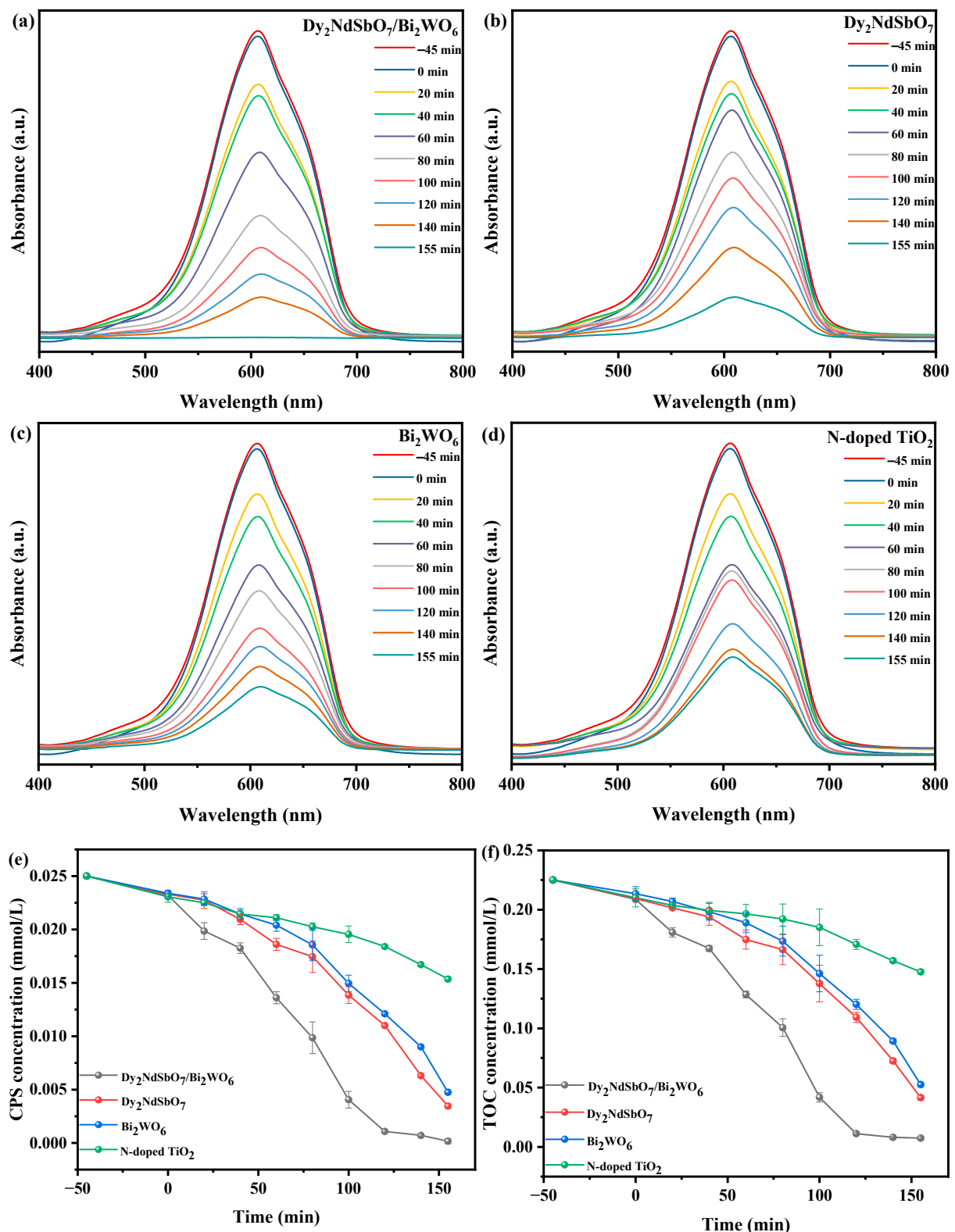


Figure 12. UV-vis absorption spectra of the CPS solution photodegraded at different times by (a) DBHP, (b) Dy_2NdSbO_7 , (c) Bi_2WO_6 , and (d) N-dT, respectively, and saturation fluctuation graphs of (e) CPS and (f) TOC during photodegradation of CPS with DBHP, Dy_2NdSbO_7 , Bi_2WO_6 , or N-dT as the catalytic sample under visible light exposure.

The saturation fluctuation graph of CPS during PDP under visible light exposure was investigated using a set of photocatalysts, including DBHP, Dy_2NdSbO_7 , Bi_2WO_6 , and

N-dT. In Figure 12e, the saturation tendency of CPS in pesticide sewage as a function of light exposure time was observed. The results clearly showed a gradual decrease in CPS saturation with gradually increasing exposure time.

The efficiency of the removal of CPS can be calculated by $(1 - \frac{C}{C_0}) \times 100\%$, where C represents the instantaneous saturation of CPS and C_0 represents the initial saturation of CPS. Analysis of the data obtained from Figure 12e demonstrated that DBHP exhibited complete removal of CPS within pesticide wastewater, achieving a reaction rate of $2.67 \times 10^{-9} \text{ mol}\cdot\text{L}^{-1}\cdot\text{s}^{-1}$ and a PHE of 0.0561% after 155 min of light exposure. Similarly, $\text{Dy}_2\text{NdSbO}_7$ achieved an RME of 86.8% for CPS, with a reaction rate of $2.33 \times 10^{-9} \text{ mol}\cdot\text{L}^{-1}\cdot\text{s}^{-1}$ and a PHE of 0.0489%. Bi_2WO_6 exhibited an RME of 81.6% for CPS, accompanied by a reaction rate of $2.19 \times 10^{-9} \text{ mol}\cdot\text{L}^{-1}\cdot\text{s}^{-1}$ and a PHE of 0.0460%. Finally, N-dT resulted in an RME of 39.2% for CPS, exhibiting a reaction rate of $1.05 \times 10^{-9} \text{ mol}\cdot\text{L}^{-1}\cdot\text{s}^{-1}$ and a PHE of 0.0221%.

The results indicated that DBHP exhibited the highest photodegradation efficiency for CPS among the studied photocatalysts. Moreover, $\text{Dy}_2\text{NdSbO}_7$ demonstrated superior photocatalytic efficacy compared to Bi_2WO_6 and N-dT. Furthermore, the photocatalytic effect of Bi_2WO_6 surpassed that of N-dT. Comparing the RME after 155 min of light exposure, DBHP displayed a 1.15 times higher RME of CPS compared to $\text{Dy}_2\text{NdSbO}_7$, 1.23 times higher than Bi_2WO_6 , and 2.55 times higher than N-dT.

Similarly, in Figure 12f, the saturation fluctuation graph of total organic carbon (TOC) during the PDP of CPS in pesticide sewage under light exposure is depicted for DBHP, $\text{Dy}_2\text{NdSbO}_7$, Bi_2WO_6 , and N-dT. The upshots revealed a gradual decrease in the saturation of TOC with increasing visible light exposure time.

The efficiency of the removal of TOC can be calculated by $(1 - \frac{\text{TOC}}{\text{TOC}_0}) \times 100\%$, where TOC represents the instantaneous saturation of total organic carbon and TOC_0 represents the initial saturation of total organic carbon. After 155 min of light exposure, DBHP achieved a TOC RME of 97.07%, $\text{Dy}_2\text{NdSbO}_7$ achieved 82.18%, Bi_2WO_6 achieved 72.24%, and N-dT achieved 35.02% RME, signifying the degradation of CPS.

In summary, the findings demonstrated that DBHP exhibited higher RME of both CPS and TOC during degradation compared to $\text{Dy}_2\text{NdSbO}_7$, Bi_2WO_6 , or N-dT. Additionally, the RME of TOC using $\text{Dy}_2\text{NdSbO}_7$ was considerably higher than that of Bi_2WO_6 or N-dT. These outcomes highlight the superior capabilities of DBHP for both mineralization and degradation of CPS, surpassing those of $\text{Dy}_2\text{NdSbO}_7$, Bi_2WO_6 , and N-dT.

The saturation fluctuation graphs of CPS and TOC during three consecutive degradation cycles using DBHP, $\text{Dy}_2\text{NdSbO}_7$, Bi_2WO_6 , or N-dT as the photocatalytic sample under visible light conditions are shown in Figures S1 and S2, respectively [105].

Figure 13 illustrates the first-order kinetic plots of CPS (Figure 13a) and TOC (Figure 13b) during the PDP of CPS using different photocatalysts (DBHP, $\text{Dy}_2\text{NdSbO}_7$, Bi_2WO_6 , and N-dT) under light exposure [106]. The kinetic constant came from the formula $(\ln \frac{C_0}{C} = k_C t)$ and $(\ln \frac{\text{TOC}_0}{\text{TOC}} = k_{\text{TOC}} t)$, where C_0 and C represented the initial saturation and reaction saturation of CPS and TOC_0 and TOC represented the initial saturation and reaction saturation of total organic carbon. k_C values, which were obtained from the dynamic CPS saturation versus light exposure time curves, were determined as 0.021 min^{-1} , 0.0089 min^{-1} , 0.0073 min^{-1} , and 0.0023 min^{-1} for DBHP, $\text{Dy}_2\text{NdSbO}_7$, Bi_2WO_6 , and N-dT, respectively. Similarly, k_{TOC} values, which were derived from the dynamic TOC saturation versus light exposure time curves, were calculated as 0.0205 min^{-1} , 0.0076 min^{-1} , 0.0064 min^{-1} , and 0.002 min^{-1} for DBHP, $\text{Dy}_2\text{NdSbO}_7$, Bi_2WO_6 , and N-dT, respectively. Importantly, k_{TOC} values were lower than k_C values for all catalysts, indicating the formation of photodegradation intermediates during the PDP. DBHP demonstrated significantly higher mineralization efficiency for CPS degradation compared to the other samples.

In Figure S3, the first-order kinetic plots of CPS and TOC during the PDP of CPS with DBHP (Figure S3a,b), $\text{Dy}_2\text{NdSbO}_7$ (Figure S3c,d), Bi_2WO_6 (Figure S3e,f), or N-dT (Figure S3g,h) as the photocatalytic sample under visible light conditions in three consecutive degradation cycles are showcased [107].

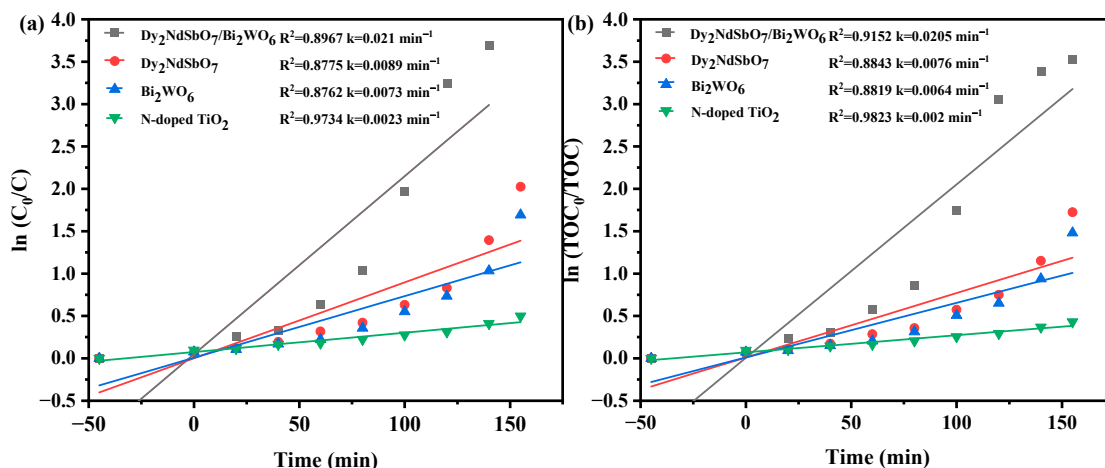


Figure 13. Observed first-order kinetics plots for (a) CPS and (b) TOC during PDP of CPS with DBHP, Dy_2NdSbO_7 , Bi_2WO_6 , or N-dT as the photocatalytic sample under light exposure.

3.6.2. Comparison of Photocatalytic Activity

In order to substantiate the distinctiveness and significance of our study, a thorough comparative analysis was conducted. Table 4 presents a comprehensive overview of pertinent research in this field, emphasizing the exceptional efficiency of CPS degradation achieved utilizing DBHP as the photocatalyst. The findings unequivocally demonstrate the superior photocatalytic efficacy of DBHP over other catalysts, underscoring its remarkable catalytic potential in this specialized domain. These results not only underscore the pivotal role of DBHP in enhancing the rate of CPS PDP but also contribute significantly to the broader field of photocatalysis, making them of considerable importance.

Table 4. Comparison of photocatalytic efficacy of DBHP with other reported photocatalysts in PDP of CPS.

Photocatalyst	Radiation	Irradiation Time (min)	Pesticide	Removal Rate (%)	Ref.
Ni-doped ZnO-TiO ₂	UV	140	Chlorpyrifos	92.66	[108]
Fe-ZnO nanocomposite	UV	60	Chlorpyrifos	81.4	[109]
Ni-doped ZnO-TiO ₂	Simulated solar light	140	Chlorpyrifos	75.22	[108]
CuO/TiO ₂	Visible light	90	Chlorpyrifos	60	[24]
TiO ₂ /PANI	Visible light	90	Chlorpyrifos	82	[24]
TiO ₂ nanoparticles	Visible light	1440	Chlorpyrifos	80	[62]
CuO-ZnO	Visible light	240	Chlorpyrifos	81	[61]
Dy_2NdSbO_7	Visible light	155	Chlorpyrifos	86.8	This study
DBHP	Visible light	155	Chlorpyrifos	100	This study

3.6.3. Impact of Photocatalytic Activity Influenced by Different Factors

Figure 14a illustrates the impact of different pH values on the removal efficiency of CPS using DBHP as the catalyst under visible light conditions and in darkness [110]. Remarkably, DBHP exhibited exceptional and consistent degradation efficiency towards CPS under visible light exposure for pH values of 3, 7, and 11. The results depicted in Figure 14a indicated that CPS degradation reached 99.2%, 100%, or 98.8% after 155 min of visible light exposure for pH values of 3, 7, or 11, respectively. Furthermore, the results obtained from Figure 14a indicated that there was an equilibrium between detachment and attachment after 45 min of dark reaction, with no significant change in CPS saturation observed under dark conditions for pH values of 3, 7, or 11, respectively. Therefore,

different pH values had no influence on the removal efficiency of CPS using DBHP as the sample either under visible light exposure or darkness.

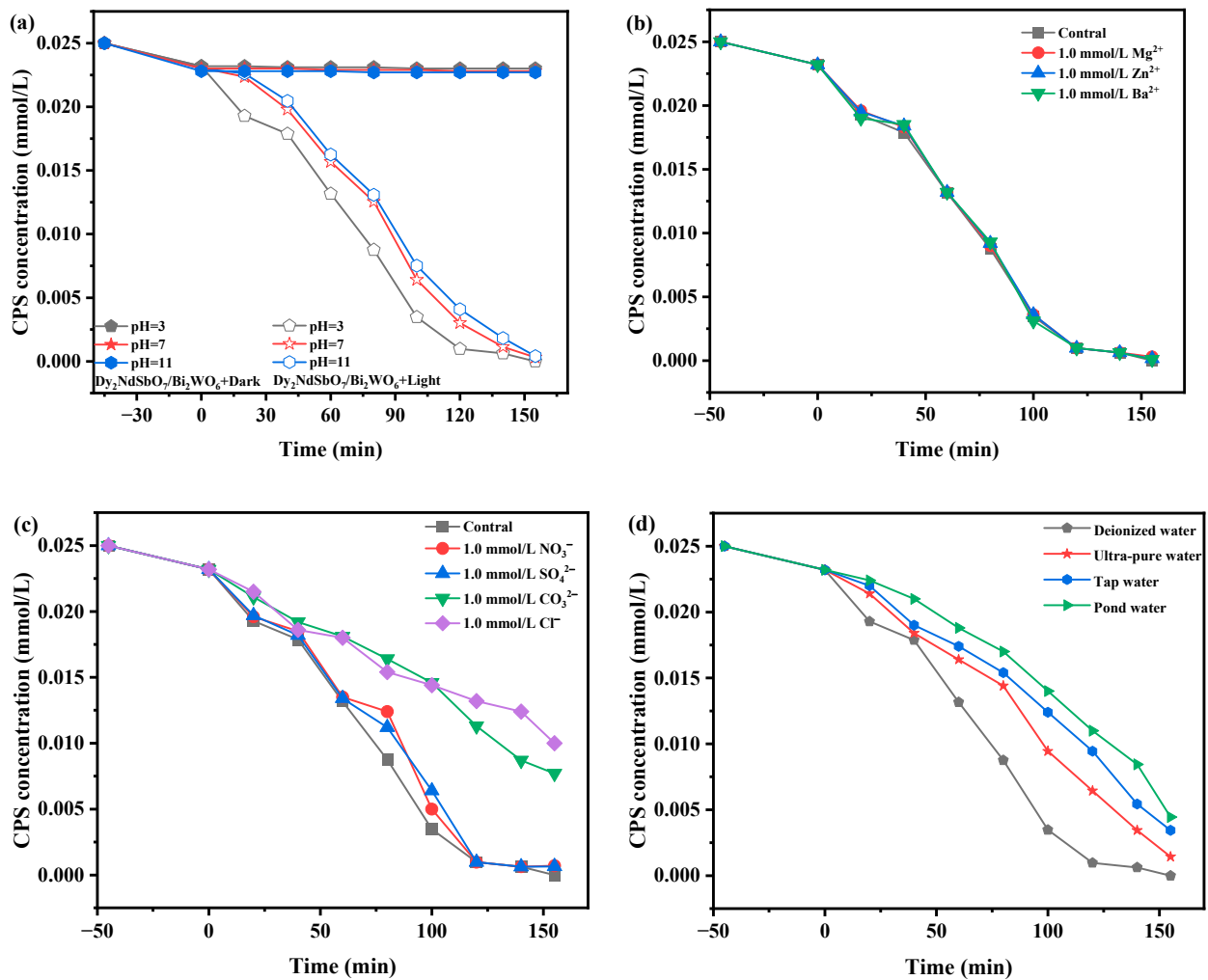


Figure 14. The effect of different (a) pH values, (b) metal ions, (c) anions, and (d) different water matrices on CPS degradation with DBHP as photocatalytic sample under visible light exposure.

Figure 14b illustrated the influence of different metal ions on the degradation efficiency of CPS using DBHP as the sample under visible light conditions [110]. Ultrapure water containing various metal ions was introduced into the photocatalytic system. The results depicted in Figure 14b confirm the effective degradation of CPS using DBHP as the sample under visible light exposure. The saturation of CPS gradually decreased with increasing visible light exposure duration. Moreover, Figure 14b demonstrated that the removal efficiency of CPS reached 100% after 155 min of visible light exposure, when DBHP was used as the sample. Additionally, the presence of 1 mmol/L Mg^{2+} , 1 mmol/L Zn^{2+} , or 1 mmol/L Ba^{2+} metal ions resulted in removal efficiencies of CPS of 98.8%, 99.4%, and 99.6%, respectively, when DBHP was utilized as the sample under visible light exposure. Notably, these metal ions did not significantly inhibit the photocatalytic degradation compared to the removal efficiency of CPS without the addition of any additional metal ions, when DBHP was used as the sample under visible light conditions.

To simulate diverse water sources, ultrapure water supplemented with various anions was incorporated in the photocatalytic reaction system. And experimental investigations were conducted to evaluate its impact on CPS degradation under visible light conditions. Notably, Figure 14c displays a gradual decrease in CPS saturation over increasing visible light exposure duration. Impressively, after 155 min of visible light exposure, the utilization

of DBHP as the sample achieved a CPS removal efficiency of 100%. Furthermore, the introduction of 1 mmol/L NO_3^- into the photocatalytic reaction system using DBHP resulted in a CPS removal efficiency of 97.2% following 155 min of visible light exposure. Similarly, the addition of 1 mmol/L SO_4^{2-} into the photocatalytic reaction system with DBHP yielded a CPS removal efficiency of 97.4% after 155 min of visible light exposure. Conversely, the inclusion of 1 mmol/L CO_3^{2-} and Cl^- into the photocatalytic reaction system resulted in CPS removal efficiencies of 69.2% and 60.0%, respectively, after 155 min of visible light exposure utilizing DBHP as the sample. These findings underscored the substantial impact of Cl^- ions present in the water source on CPS degradation. The higher proportion of Cl^- resulted in the significant consumption of $\bullet\text{OH}$ and photoexcited holes, ultimately diminishing free radicals' availability and hampering the PDP. Water sources with higher proportions of NO_3^- or SO_4^{2-} exhibited a lesser inhibitory effect on the PDP of CPS. This is due to the fact that NO_3^- or SO_4^{2-} only consume photoexcited holes within the photocatalytic reaction system, thus resulting in a milder inhibitory effect [110].

The photodegradation profiles of CPS in different water matrices are presented in Figure 14d. Significantly high removal efficiency of CPS was observed under visible light conditions in deionized water, resulting in complete degradation (100%). This can be attributed to the low conductivity of deionized water, indicating lower levels of dissolved solids and ions that can promote the immediate degradation of organic compounds through the generation of reactive radicals. The removal efficiency of CPS under visible light was determined to be 94.4% and 86.4% in tap water and ultra-pure water, respectively, which can be ascribed to the comparatively lower levels of dissolved solids and organic matter in these water samples [111]. Moreover, it is important to note that the presence of dissolved organic matter, commonly found in pond water, may function as scavengers of holes and hydroxyl radicals, resulting in reduced oxidant production and unfavorable effects on the overall photocatalytic removal of target pollutants. The removal efficiency of CPS in this case was 82.4% [112].

3.7. Property Characterization

Figure 15a,b investigated the influence of various radical scavengers, including BQ, IPA, and EDTA, on the RME of CPS using DBHP as the photocatalyst under visible light exposure. Figure S4 showcases the impact of different scavengers on CPS saturation with DBHP as a photocatalyst under visible light exposure for triplicate experiments. These scavengers were introduced in the initial period of the PDP to identify the active species involved in the degradation process. The saturation of BQ, IPA, or EDTA used was 0.05 mmol L^{-1} , with an added volume of 3 mL. The presence of BQ, IPA, or EDTA resulted in a reduction of the average CPS RME by 48.8%, 36.8%, and 22%, respectively, compared to the control group. These findings indicated the participation of superoxide anions ($\bullet\text{O}_2^-$), hydroxyl radicals ($\bullet\text{OH}$), and holes (h^+) as active radicals in the CPS degradation process. Among these active radicals, $\bullet\text{O}_2^-$ exhibited the highest oxidation removal capability, facilitating the elimination of CPS in pesticide sewage when DBHP carried out the role of the photocatalytic sample. The ascending order of oxidation removal ability in degrading CPS was $\bullet\text{O}_2^- > \bullet\text{OH} > \text{h}^+$.

To investigate the generation of $\bullet\text{O}_2^-$ radicals and $\bullet\text{OH}$ radicals during the PDP, Electron Paramagnetic Resonance (EPR) analysis was employed [113]. In our study, a solution consisting of 20 mg of the DBHP sample, 90 μL of DMPO (1 mol/L), and 1 mL of deionized water was prepared to detect the $\bullet\text{OH}$ radicals or $\bullet\text{O}_2^-$ radicals produced by DBHP. Figure 16 presents the EPR spectrum for DMPO $\bullet\text{O}_2^-$ and DMPO $\bullet\text{OH}$ when DBHP was used as the photocatalytic sample. Upon 10 min of exposure to visible light, a distinct DMPO $\bullet\text{O}_2^-$ signal was observed in the EPR spectrum, featuring four strong peaks with an equal intensity ratio of 1:1:1:1. This observation indicated the presence of $\bullet\text{O}_2^-$ radicals. Furthermore, the EPR spectrum also revealed a four-line signal with a 1:2:2:1 intensity ratio, corresponding to the DMPO $\bullet\text{OH}$ signal, after visible light exposure. These findings suggested the concurrent production of $\bullet\text{O}_2^-$ radicals and $\bullet\text{OH}$ radicals. Moreover, the

higher relative intensity of the EPR signals for these reactive radicals indicates a higher yield of these species. Specifically, the yield of $\bullet\text{O}_2^-$ radicals was higher than that of $\bullet\text{OH}$ radicals. These outcomes aligned with the results obtained from the radical-scavenger experiments discussed earlier.

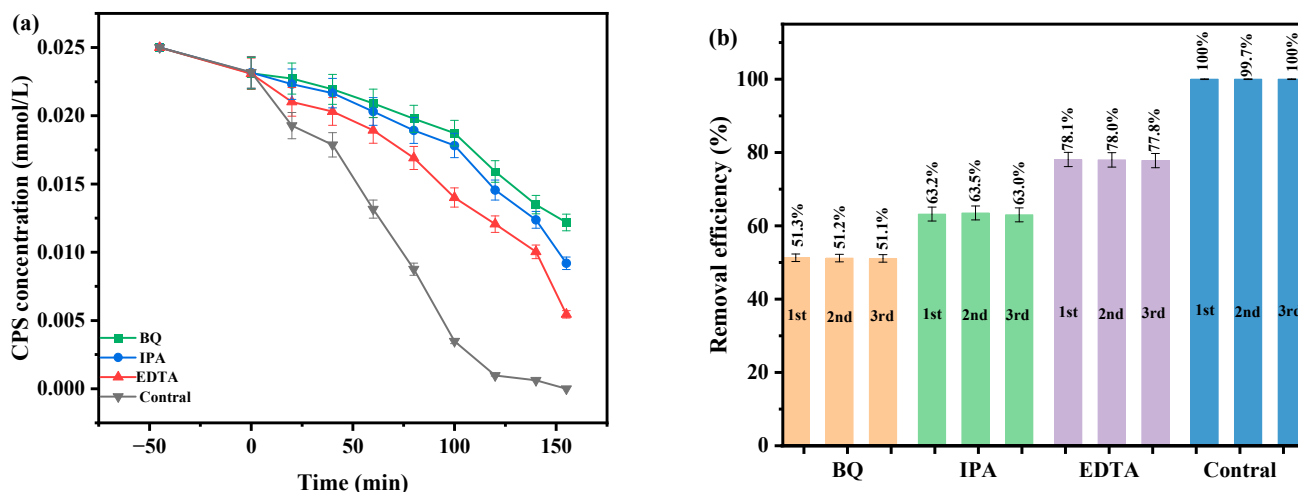


Figure 15. Effect of different radical scavengers on (a) CPS saturation and (b) RME of CPS.

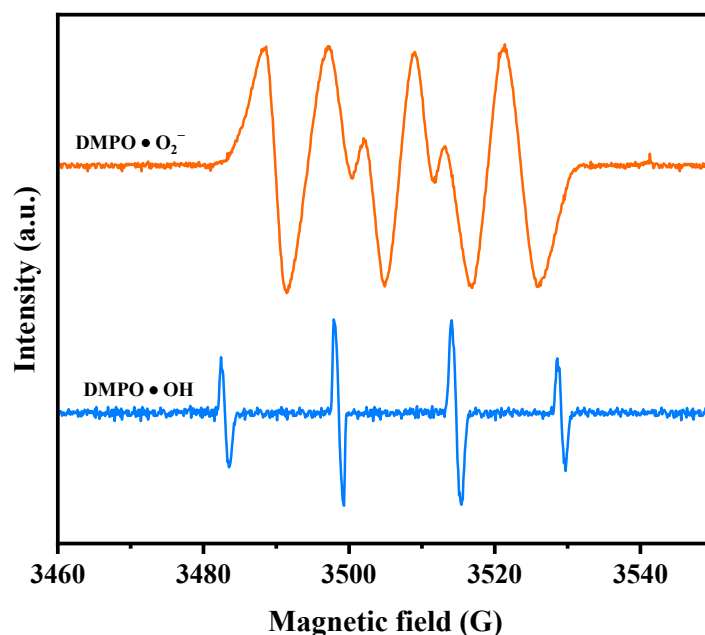


Figure 16. EPR spectrum for $\text{DMPO} \bullet \text{O}_2^-$ and $\text{DMPO} \bullet \text{OH}$ over DBHP.

To gain comprehensive insights into the interfacial carrier dynamics and recombination, a series of effective characterization techniques were employed. The Photoluminescence (PL) spectrum and Time-Resolved Photoluminescence (TRPL) spectra of $\text{Dy}_2\text{NdSbO}_7$, Bi_2WO_6 , and DBHP are depicted in Figure 17a–d, respectively. PL spectroscopy is a valuable technique for investigating the optical properties, carrier behavior, and photocatalytic effect of the heterostructure sample [114,115]. Higher PL intensities typically indicate faster recombination rates of the PCC, which in turn result in a lower photocatalytic effect. In Figure 17a, it can be observed that the DBHP exhibited the minimum radiative intensity, suggesting the recombination of the PCC is greatly restricted, owing to the more efficient charge separation. The $\text{Dy}_2\text{NdSbO}_7$ sample displayed a higher radiative intensity compared to DBHP, while Bi_2WO_6 exhibited an even higher radiative intensity than both

Dy₂NdSbO₇ and DBHP. The forementioned results indicated that the formation of the heterostructure sample can effectively enhance the photocatalytic effect towards CPS. Furthermore, this provided further evidence that DBHP possesses the highest photocatalytic effect among the Dy₂NdSbO₇ and Bi₂WO₆ samples. The TRPL spectra of Dy₂NdSbO₇, Bi₂WO₆, and DBHP in Figure 17b–d were fitted by the following double-exponential decay Equation (5) [116]:

$$I(t) = I_0 + A_1 \exp\left(-\frac{t}{\tau_1}\right) + A_2 \exp\left(-\frac{t}{\tau_2}\right) \quad (5)$$

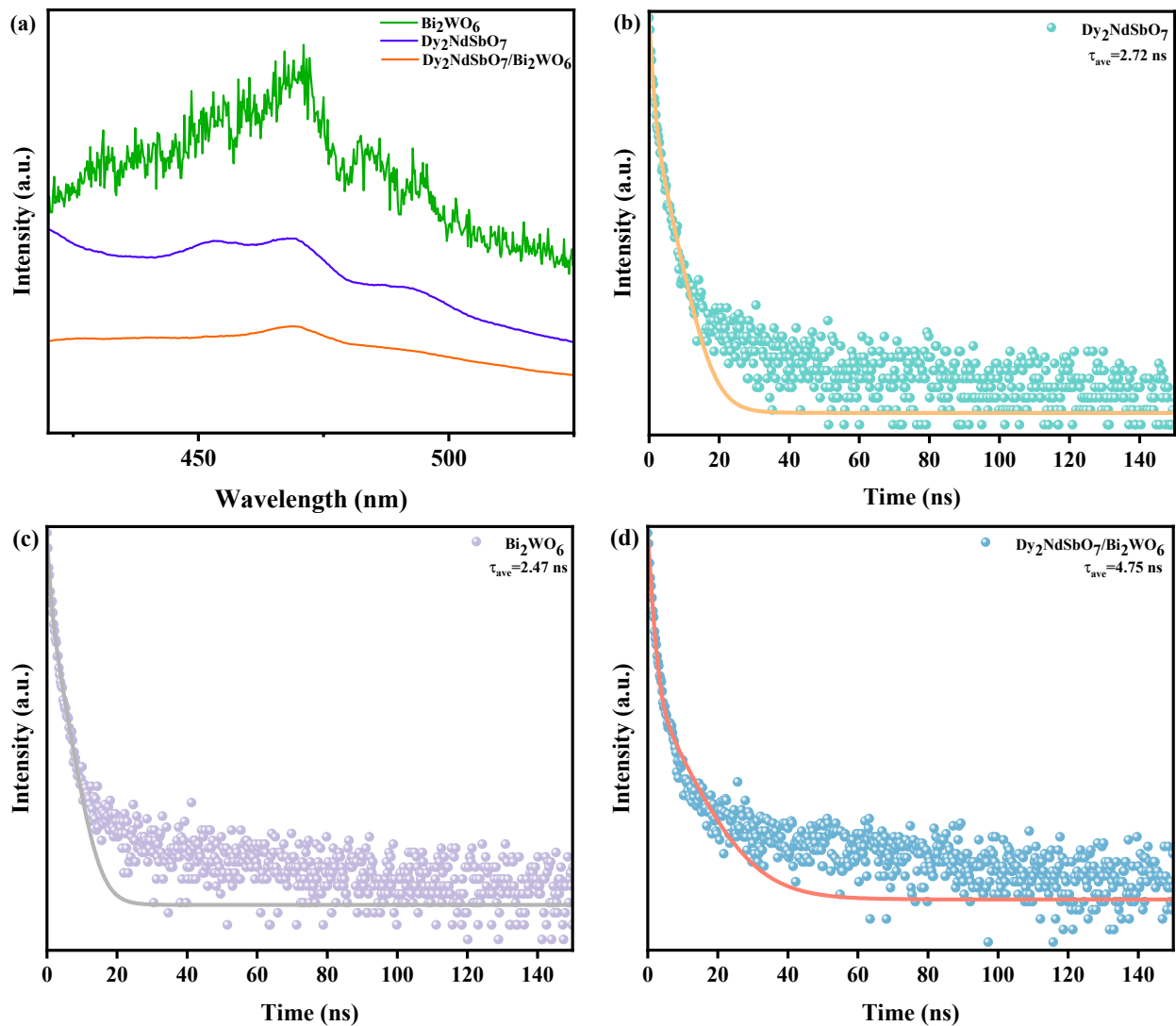


Figure 17. (a) PL spectrum of DBHP, Dy₂NdSbO₇, and Bi₂WO₆, and TRPL spectra of (b) Dy₂NdSbO₇, (c) Bi₂WO₆, and (d) DBHP.

In the provided equation, τ_1 and τ_2 represent the first and second-order decay times, and A_1 and A_2 are weighting coefficients of each decay channel [117]. To determine the average PCC lifetime (τ_{ave}), the following Equation (6) was utilized [118]:

$$\tau_{ave} = (A_1 \tau_1^2 + A_2 \tau_2^2) / (A_1 \tau_1 + A_2 \tau_2) \quad (6)$$

The fitted lifetimes and the corresponding parameters are given in Table S1. DBHP ($\tau_1 = 1.1089$ ns, $\tau_2 = 8.6413$ ns, $\tau_{ave} = 4.7516$ ns) presented a much higher PCC lifetime than Dy₂NdSbO₇ ($\tau_1 = 0.8808$ ns, $\tau_2 = 3.8272$ ns, $\tau_{ave} = 2.7208$ ns) and Bi₂WO₆ ($\tau_1 = 0.6405$ ns,

$\tau_2 = 3.0289$ ns, $\tau_{ave} = 2.4700$ ns), which indicated that DBHP was endowed with the unbeatable photocatalytic efficacy over the individual $\text{Dy}_2\text{NdSbO}_7$ and Bi_2WO_6 .

The influence of the prepared sample on the efficiency of PCC separation was studied using photocurrent and electrochemical impedance spectroscopy (EIS) techniques. Figure 18a illustrates the transient photocurrent responses of DBHP, as well as individual $\text{Dy}_2\text{NdSbO}_7$ and Bi_2WO_6 samples. As evident from the results, DBHP exhibited the highest intensity of photocurrent response compared to $\text{Dy}_2\text{NdSbO}_7$ and Bi_2WO_6 . This reinforced photocurrent response intensity in DBHP can be attributed to the efficient diffusion of photoexcited electrons, along with the rapid transfer of photoexcited holes to the surface of Bi_2WO_6 . This phenomenon occurred due to the electric potential difference between the valence band of $\text{Dy}_2\text{NdSbO}_7$ and Bi_2WO_6 within the DBHP composite. Consequently, the intensified photocurrent response in DBHP indicated effective separation of PCC and their prolonged lifetime compared to $\text{Dy}_2\text{NdSbO}_7$ and Bi_2WO_6 during the PDP. These observations further elucidated the superior photocatalytic efficacy achieved with DBHP [119,120].

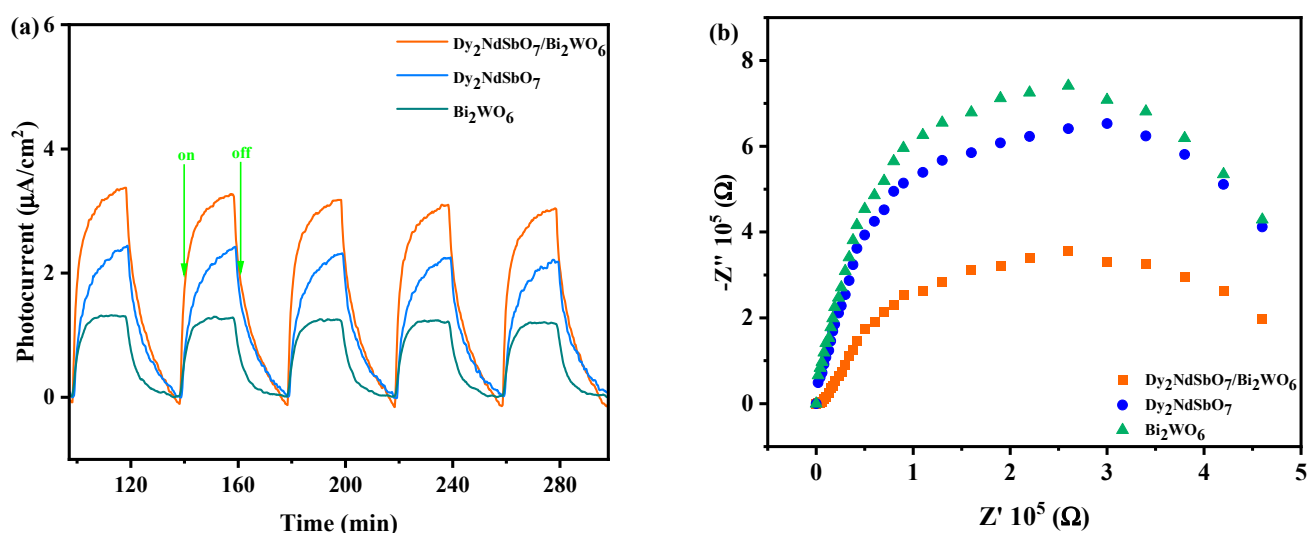


Figure 18. (a) Transient photocurrent and (b) Nyquist impedance plots of DBHP, $\text{Dy}_2\text{NdSbO}_7$, and Bi_2WO_6 .

The electrochemical impedance spectroscopy (EIS) is another significant characterization technique that provides insights into the migration process of photogenerated carriers at the interfaces of two single-crystal photocatalysts forming a heterojunction [121,122]. In this study, the arc radius in the Nyquist impedance plot was used to evaluate photoinduced carrier migration efficiency in the prepared photocatalysts. A smaller arc radius indicates higher efficiency. The Nyquist impedance plots of the DBHP, $\text{Dy}_2\text{NdSbO}_7$, and Bi_2WO_6 samples are showcased in Figure 18b. Analysis of Figure 18b revealed a trend in the arc radius diameter: $\text{Bi}_2\text{WO}_6 > \text{Dy}_2\text{NdSbO}_7 > \text{DBHP}$. This suggested that the DBHP sample exhibited superior photocatalytic efficacy by efficiently separating PCC, improving interfacial charge mobility and generating more radicals involved in PDP compared to $\text{Dy}_2\text{NdSbO}_7$ and Bi_2WO_6 . These findings aligned with the results presented in Figures 12, S1, 17 and 18a.

3.8. Analysis of Possible Degradation Mechanisms

Figure 19 showcases the UPS spectra of $\text{Dy}_2\text{NdSbO}_7$ and Bi_2WO_6 and Figure 20 showcases the possible photocatalytic degradation mechanism of CPS with DBHP under visible light exposure. Ultraviolet Photoelectron Spectroscopy (UPS) measurements were performed to determine the ionization potential of $\text{Dy}_2\text{NdSbO}_7$ and Bi_2WO_6 . The potentials of the VB for both p-type and n-type semiconductor samples could be calculated using the UPS analysis [123]. The onset (E_i) and cutoff (E_{cutoff}) binding energies for both

semiconductor samples are showcased in Figure 19. These numerical values were measured as 1.378 eV and 19.865 eV for $\text{Dy}_2\text{NdSbO}_7$, and 0.748 eV and 20.120 eV for Bi_2WO_6 [124]. By calculating from the excitation energy (approximately 21.2 eV), the ionization potential of $\text{Dy}_2\text{NdSbO}_7$ and Bi_2WO_6 was determined as 2.713 eV and 1.828 eV, respectively [125]. As a result, the CB potential of $\text{Dy}_2\text{NdSbO}_7$ and Bi_2WO_6 was determined as 0.143 eV and -0.632 eV, respectively. These findings provide further support to the mechanistic model proposed in this study.

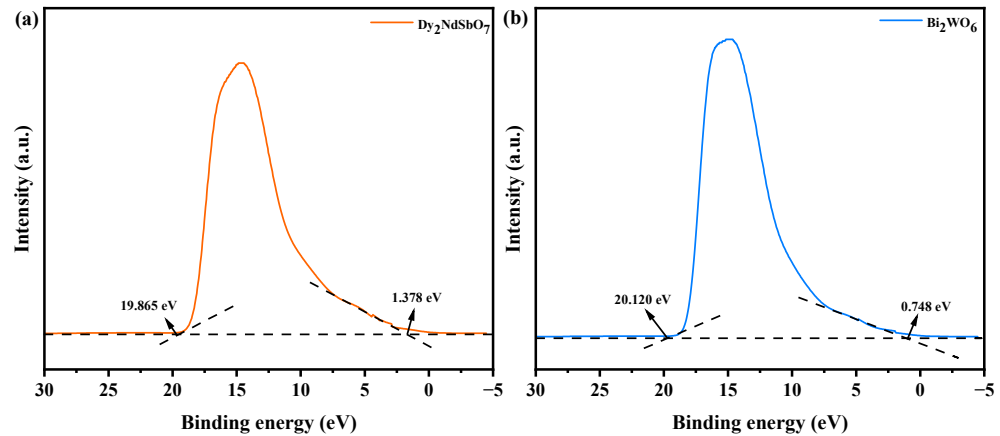


Figure 19. UPS spectra of (a) $\text{Dy}_2\text{NdSbO}_7$ and (b) Bi_2WO_6 (the intersections of the black dash lines indicated by the black arrows indicated the onset (E_i) and cutoff (E_{cutoff}) binding energy).

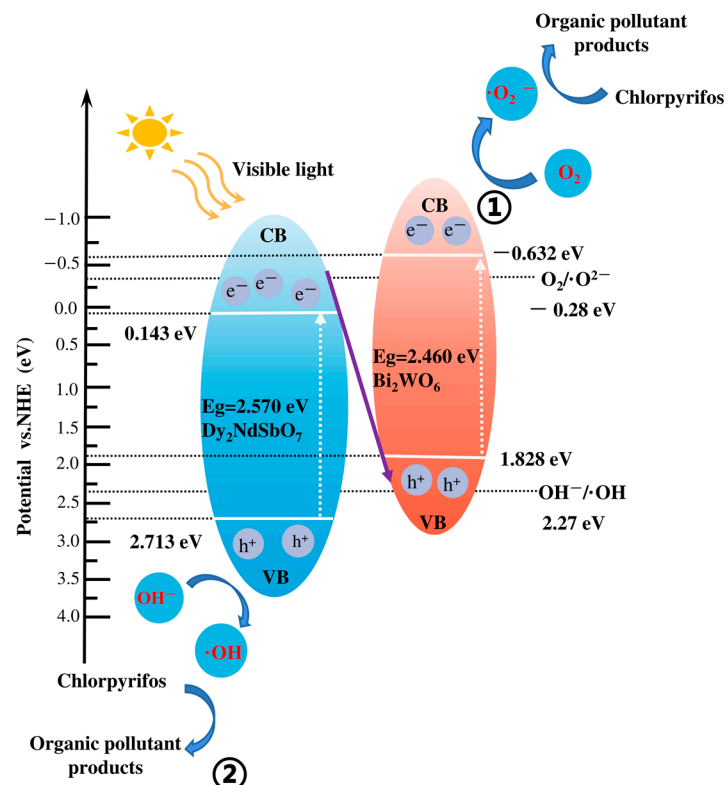


Figure 20. Possible photodegradation mechanism of CPS with DBHP as photocatalyst under visible light condition.

Despite the higher CB potential of Bi_2WO_6 compared to $\text{Dy}_2\text{NdSbO}_7$, electrons were observed to transfer from the CB of Bi_2WO_6 to the CB of $\text{Dy}_2\text{NdSbO}_7$. Similarly, due to the higher VB potential of $\text{Dy}_2\text{NdSbO}_7$ compared to Bi_2WO_6 , holes were found to transfer from the VB of $\text{Dy}_2\text{NdSbO}_7$ to the VB of Bi_2WO_6 . It is important that Lee et al. have confirmed

that different pH values would give different $\text{OH}^- / \bullet\text{OH}$ potentials and the standard potential of reactive oxygen species would be affected by the pH [30]. Therefore, the formation of $\bullet\text{OH}$ was impeded by the more positive $\text{OH}^- / \bullet\text{OH}$ potential (2.27 eV vs. NHE, pH = 7) compared to the VB potential of Bi_2WO_6 (1.829 eV) [30]. Additionally, the generation of $\bullet\text{O}_2^-$ was suppressed due to the more positive conduction band potential of $\text{Dy}_2\text{NdSbO}_7$ (0.142 eV) relative to $\text{O}_2 / \bullet\text{O}_2^-$ (-0.28 eV vs. NHE, pH = 7) [30]. However, these findings were inconsistent with the experimental results obtained through EPR analysis.

Based on the proposed photocatalytic mechanism illustrated in Figure 20, it was anticipated that the CB potential of Bi_2WO_6 (-0.591 eV) would be more negative than that of $\text{O}_2 / \bullet\text{O}_2^-$ (-0.28 eV vs. NHE, pH = 7) [126–128], signifying that electrons in the CB of Bi_2WO_6 could react with oxygen to generate $\bullet\text{O}_2^-$ for the degradation of CPS (① in Figure 20). Similarly, the VB potential of $\text{Dy}_2\text{NdSbO}_7$ (2.712 eV) was expected to be more positive than that of $\text{OH}^- / \bullet\text{OH}$ (2.27 eV vs. NHE, pH = 7) [129,130], indicating that holes in the VB of $\text{Dy}_2\text{NdSbO}_7$ could oxidize water (H_2O) or hydroxide ions (OH^-) to generate $\bullet\text{OH}$ for CPS degradation (② in Figure 20). The above analysis aligned with the experimental results obtained through EPR analysis.

Therefore, the most plausible explanation is that DBHP operates through a direct type-S photocatalytic mechanism [131,132]. In the direct type-S heterojunction, the heterostructure formed between the two samples not only retains superior redox potentials but also reduces the recombination rate of PCC. This configuration greatly enhances the photocatalytic efficacy of the heterostructure sample.

In this study, a comprehensive analysis using a Liquid Chromatograph-Mass Spectrometer (LC-MS) was conducted for investigating the degradation process of CPS. Through this meticulous analysis, a total of nine distinct intermediate products were successfully identified and characterized.

Based on our findings, we propose a mechanistic scheme illustrating the degradation pathway of CPS on the catalyst surface, as shown in Figure 21. Initially, catalytically generated hydroxyl radicals ($\bullet\text{OH}$) interact with CPS, leading to the oxidation of the P=S bond and the formation of intermediate $\text{C}_9\text{H}_{11}\text{Cl}_3\text{O}_4\text{PN}$ ($m/z = 334$) [133]. Simultaneously, oxidative processes, including ring hydroxylation and dechlorination reactions, contribute to the formation of intermediate $\text{C}_9\text{H}_{12}\text{Cl}_2\text{O}_4\text{PN}$ ($m/z = 350$) [133]. Subsequent hydrolysis transformations of intermediates $\text{C}_9\text{H}_{11}\text{Cl}_3\text{O}_4\text{PN}$ ($m/z = 334$) and $\text{C}_9\text{H}_{12}\text{Cl}_2\text{O}_4\text{PN}$ ($m/z = 350$) result in the formation of diethyl hydrogen phosphate ($m/z = 155$) as a significant intermediate [133].

Furthermore, we discovered that intermediate $\text{C}_9\text{H}_{11}\text{Cl}_3\text{O}_4\text{PN}$ ($m/z = 334$) can undergo hydrolysis, leading to the loss of two ethanol molecules and the formation of intermediate $\text{C}_7\text{H}_7\text{Cl}_3\text{O}_4\text{PN}$ ($m/z = 276$) [133,134]. Dephosphorylation of intermediate $\text{C}_7\text{H}_7\text{Cl}_3\text{O}_4\text{PN}$ ($m/z = 276$) produces 3,5,6-Trichloro-2-pyridinol ($m/z = 196$) [133,134]. It is noteworthy that the formation of trichloropyridinol and the intermediates $\text{C}_9\text{H}_{11}\text{Cl}_3\text{O}_4\text{PN}$ ($m/z = 334$), $\text{C}_7\text{H}_7\text{Cl}_3\text{O}_4\text{PN}$ ($m/z = 276$), and diethyl hydrogen phosphate ($m/z = 155$) has been previously observed in the degradation process of CPS [133,134].

Further experimental investigations revealed that trichloropyridinol undergoes successive dehydroxylation and dechlorination reactions, resulting in the formation of 3,5-dichloropyridine ($m/z = 149$) and pyridine hydrochloride ($m/z = 129$) [133,134]. Importantly, the dechlorination of pyridine hydrochloride generates pyridine ($m/z = 79$) as a key intermediate in the degradation process [133,134]. Finally, the intermediate organic species generated during the degradation process undergo further decomposition on the photocatalyst surface, ultimately resulting in the formation of crucial end products, including CO_2 , H_2O , Cl^- , NH_4^+ , NO_3^- , and PO_4^{3-} species.

The comprehensive analysis of the CPS degradation pathway on the catalyst surface conducted in this study provides valuable insights into the underlying mechanisms governing this process. Our research significantly contributes to a deeper understanding of catalytic degradation processes and offers promising opportunities for the development of efficient and environmentally friendly strategies for CPS contamination degradation.

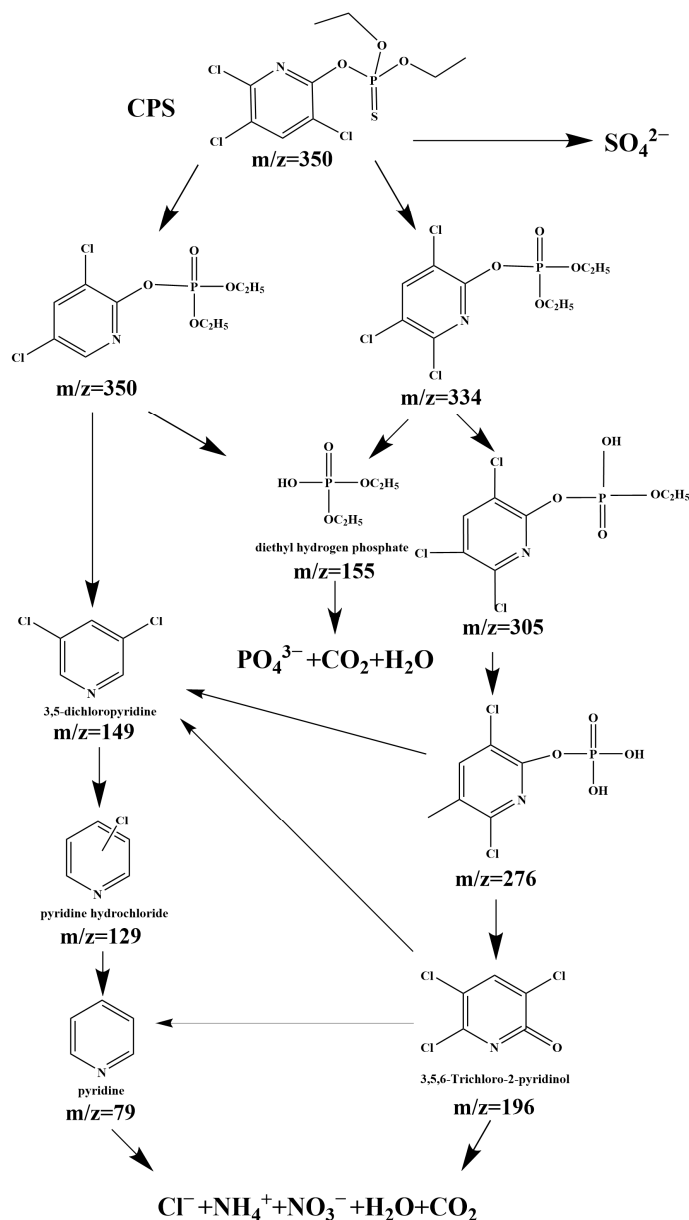


Figure 21. Suggested photodegradation pathway scheme for CPS under visible light condition with DBHP as photocatalyst.

4. Conclusions

In summary, this study successfully synthesized the novel $\text{Dy}_2\text{NdSbO}_7$ photocatalyst using the hydrothermal synthesis technique. The novel $\text{Dy}_2\text{NdSbO}_7$ material exhibited a pure phase with a pyrochlore structure, cubic crystal system, and space group $\text{Fd}\bar{3}\text{m}$. Characterization techniques such as XRD, FTIR, Raman, UV-vis, XPS, and TEM-EDS confirmed its structural and compositional properties. In addition, DBHP was successfully prepared for the first time through a facile solvothermal method. The fabrication of a heterostructure between $\text{Dy}_2\text{NdSbO}_7$ and Bi_2WO_6 played a pivotal role in reinforcing the photocatalytic efficacy, resulting in remarkable advancements in pollutant degradation. Notably, the developed DBHP exhibited outstanding performance in removing CPS from pesticides wastewater. Within a remarkably short time of 155 min, DBHP achieved a remarkable RME of CPS saturation (up to 100%) and TOC saturation (up to 97.07%). Comparing DBHP with $\text{Dy}_2\text{NdSbO}_7$, Bi_2WO_6 , and N-dT demonstrated a higher CPS RME of 1.15 times, 1.23 times, and 2.55 times, respectively. The superior photocatalytic activity of DBHP can be credited to its high charge separation efficiency and low recombination

of PCC. The formation of the heterojunction between $\text{Dy}_2\text{NdSbO}_7$ and Bi_2WO_6 facilitated good performance of charge migration and propelled the output of free radicals, thereby enhancing the degradation of CPS. The results of the study revealed that $\bullet\text{O}_2^-$ radicals were the primary reactive species responsible for the degradation of CPS, while $\bullet\text{OH}$ and h^+ radicals also participated in the degradation process. Moreover, this study proposed a plausible degradation pathway and mechanism for CPS, providing valuable insights into the photocatalytic process.

Overall, the successful synthesis of the $\text{Dy}_2\text{NdSbO}_7$ photocatalyst and the development of DBHP provide a promising approach for treating wastewater contaminated with CPS. These findings make a significant contribution to the progress of photocatalytic technology and offer precious discernments for the progress and development of highly efficient photocatalytic nanophase materials for the degradation of pollutants.

Supplementary Materials: The following supporting information can be downloaded at: <https://www.mdpi.com/article/10.3390/cryst14010055/s1>, Figure S1: Saturation fluctuation graphs of CPS during PDP of CPS in pesticides sewage with (a) DBHP, (b) $\text{Dy}_2\text{NdSbO}_7$, (c) Bi_2WO_6 , or (d) N-dT as photocatalytic sample under visible light exposure for three cycle degradation detections; Figure S2: Saturation fluctuation graphs of TOC during PDP of CPS in pesticides sewage with (a) DBHP, (b) $\text{Dy}_2\text{NdSbO}_7$, (c) Bi_2WO_6 , or (d) N-dT as photocatalytic sample under visible light exposure for three cycle degradation detection; Figure S3: Observed first-order kinetic plots for CPS and TOC during photodegradation of CPS with (a,b) DBHP, (c,d) $\text{Dy}_2\text{NdSbO}_7$, (e,f) Bi_2WO_6 , or (g,h) N-dT as photocatalytic sample under visible light exposure for three cycle degradation detection; Figure S4: Effect of (a) without scavenger, (b) EDTA, (c) IPA, and (d) BQ on CPS saturation with DBHP as photocatalytic sample under visible light exposure for triplicate experiments; Table S1: Fitted results of TRPL curves of $\text{Dy}_2\text{NdSbO}_7$, Bi_2WO_6 , and DBHP. The calculation process of the value of the E_{CB} of $\text{Dy}_2\text{NdSbO}_7$ and Bi_2WO_6 .

Author Contributions: J.L. (Jingfei Luan): conceptualization, data curation, formal analysis, investigation, methodology, software, visualization, writing-original draft preparation, writing-review and editing, validation. L.H.: software, data curation, methodology, writing-original draft preparation, validation. Y.Y.: formal analysis, investigation, writing-original draft preparation, validation, investigation. Y.W.: software, visualization, validation. G.Y.: methodology, software, validation, investigation. J.L. (Jun Li): formal analysis, methodology, writing-original draft preparation. All authors have read and agreed to the published version of the manuscript.

Funding: This study was supported by the Free Exploring Key Item of the Natural Science Foundation of the Science and Technology Bureau of Jilin Province of China (Grant No. YDZJ202101ZYTS161).

Institutional Review Board Statement: Not applicable.

Informed Consent Statement: Not applicable.

Data Availability Statement: Data are contained within the article.

Conflicts of Interest: The authors declare no conflicts of interest.

References

1. Zhang, Y.J.; Zhou, B.H.; Chen, H.L.; Yuan, R.F. Heterogeneous photocatalytic oxidation for the removal of organophosphorus pollutants from aqueous solutions: A review. *Sci. Total Environ.* **2023**, *856*, 159048. [[CrossRef](#)] [[PubMed](#)]
2. Gordi, Z.; Bayat, A. Development and synthesis of a metal-organic framework on metal-organic framework composite as a novel catalyst for photodegradation of two organophosphorus pesticides under visible light. *React. Kinet. Mech. Catal.* **2023**, *136*, 1673–1688. [[CrossRef](#)]
3. Sibmah, S.; Kirupavasam, E.K. An efficient photocatalytic degradation of Quinalphos pesticide under visible light using zinc oxide/magnesium oxide nanocomposites as a novel photocatalyst. *Indian J. Chem.* **2022**, *61*, 901–908. [[CrossRef](#)]
4. Mumtaz, N.; Javaid, A.; Imran, M.; Latif, S.; Hussain, N.; Nawaz, S.; Bilal, M. Nanoengineered metal-organic framework for adsorptive and photocatalytic mitigation of pharmaceuticals and pesticide from wastewater. *Environ. Pollut.* **2022**, *308*, 119690. [[CrossRef](#)] [[PubMed](#)]
5. Fu, H.Y.; Tan, P.; Wang, R.J.; Li, S.N.; Liu, H.Z.; Yang, Y.; Wu, Z.L. Advances in organophosphorus pesticides pollution: Current status and challenges in ecotoxicological, sustainable agriculture, and degradation strategies. *J. Hazard. Mater.* **2022**, *424*, 127494. [[CrossRef](#)] [[PubMed](#)]

6. Li, G.L.; Wen, A.; Liu, J.H.; Wu, D.; Wu, Y.N. Facile extraction and determination of organophosphorus pesticides in vegetables via magnetic functionalized covalent organic framework nanocomposites. *Food Chem.* **2021**, *337*, 127974. [[CrossRef](#)]
7. Sharma, A.; Shukla, A.; Attri, K.; Kumar, M.; Kumar, P.; Sutte, A.; Singh, G.; Barnwal, R.P.; Singla, N. Global trends in pesticides: A looming threat and viable alternatives. *Ecotoxicol. Environ. Saf.* **2020**, *201*, 110812. [[CrossRef](#)] [[PubMed](#)]
8. Zhu, X.Y.; Li, B.; Yang, J.; Li, Y.S.; Zhao, W.R.; Shi, J.L.; Gu, J.L. Effective Adsorption and Enhanced Removal of Organophosphorus Pesticides from Aqueous Solution by Zr-Based MOFs of UiO-67. *ACS Appl. Mater. Interfaces* **2015**, *7*, 223–231. [[CrossRef](#)]
9. Gilani, R.A.; Rafique, M.; Rehman, A.; Munis, M.F.H.; Rehman, S.U.; Chaudhary, H.J. Biodegradation of chlorpyrifos by bacterial genus *Pseudomonas*. *J. Basic Microbiol.* **2016**, *56*, 105–119. [[CrossRef](#)]
10. Yadav, M.; Srivastva, N.; Singh, R.S.; Upadhyay, S.N.; Dubey, S.K. Biodegradation of chlorpyrifos by *Pseudomonas* sp. in a continuous packed bed bioreactor. *Bioresour. Technol.* **2014**, *165*, 265–269. [[CrossRef](#)]
11. Sasikala, C.; Jiwal, S.; Rout, P.; Ramya, M. Biodegradation of chlorpyrifos by bacterial consortium isolated from agriculture soil. *World J. Microbiol. Biotechnol.* **2012**, *28*, 1301–1308. [[CrossRef](#)] [[PubMed](#)]
12. Gearhart, D.A.; Sickles, D.W.; Buccafusco, J.J.; Prendergast, M.A.; Terry, A.V. Chlorpyrifos, chlorpyrifos-oxon, and diisopropylfluorophosphate inhibit kinesin-dependent microtubule motility. *Toxicol. Appl. Pharmacol.* **2007**, *218*, 20–29. [[CrossRef](#)] [[PubMed](#)]
13. Steevens, J.A.; Benson, W.H. Toxicokinetic interactions and survival of *Hyalella azteca* exposed to binary mixtures of chlorpyrifos, dieldrin, and methyl mercury. *Aquat. Toxicol.* **2001**, *51*, 377–388. [[CrossRef](#)] [[PubMed](#)]
14. Steevens, J.A.; Benson, W.H. Interactions of chlorpyrifos and methyl mercury: A mechanistic approach to assess chemical mixtures. *Mar. Environ. Res.* **2000**, *50*, 113–117. [[CrossRef](#)] [[PubMed](#)]
15. Thind, P.S.; Kumari, D.; John, S. TiO₂/H₂O₂ mediated UV photocatalysis of Chlorpyrifos: Optimization of process parameters using response surface methodology. *J. Environ. Chem. Eng.* **2018**, *6*, 3602–3609. [[CrossRef](#)]
16. Sarangapani, C.; Misra, N.N.; Milosavljevic, V.; Bourke, P.; O'Regan, F.; Cullen, P.J. Pesticide degradation in water using atmospheric air cold plasma. *J. Water Process Eng.* **2016**, *9*, 225–232. [[CrossRef](#)]
17. Chakma, S.; Moholkar, V.S. Mechanistic analysis of hybrid sono-photo-ferrioxalate system for decolorization of azo dye. *J. Taiwan Inst. Chem. E* **2016**, *60*, 469–478. [[CrossRef](#)]
18. Ahmad, T.; Rafatullah, M.; Ghazali, A.; Sulaiman, O.; Hashim, R.; Ahmad, A. Removal of Pesticides from Water and Wastewater by Different Adsorbents: A Review. *J. Environ. Sci. Health Part C Environ. Carcinog. Ecotoxicol. Rev.* **2010**, *28*, 231–271. [[CrossRef](#)]
19. Agarwal, S.; Tyagi, I.; Gupta, V.K.; Dehghani, M.H.; Bagheri, A.; Yetilmezsoy, K.; Amrane, A.; Heibati, B.; Rodriguez-Couto, S. Degradation of azinphos-methyl and chlorpyrifos from aqueous solutions by ultrasound treatment. *J. Mol. Liq.* **2016**, *221*, 1237–1242. [[CrossRef](#)]
20. Soltani-nezhad, F.; Saljooqi, A.; Mostafavi, A.; Shamspur, T. Synthesis of Fe₃O₄/CdS-ZnS nanostructure and its application for photocatalytic degradation of chlorpyrifos pesticide and brilliant green dye from aqueous solutions. *Ecotoxicol. Environ. Saf.* **2020**, *189*, 109886. [[CrossRef](#)]
21. Merci, S.; Saljooqi, A.; Shamspur, T.; Mostafavi, A. Investigation of photocatalytic chlorpyrifos degradation by a new silica mesoporous material immobilized by WS₂ and Fe₃O₄ nanoparticles: Application of response surface methodology. *Appl. Organomet. Chem.* **2020**, *34*, e5343. [[CrossRef](#)]
22. Zangiabadi, M.; Shamspur, T.; Saljooqi, A.; Mostafavi, A. Evaluating the efficiency of the GO-Fe₃O₄/TiO₂ mesoporous photocatalyst for degradation of chlorpyrifos pesticide under visible light irradiation. *Appl. Organomet. Chem.* **2019**, *33*, e4813. [[CrossRef](#)]
23. Mansourian, R.; Mousavi, S.M.; Alizadeh, S.; Sabbaghi, S. CeO₂/TiO₂/SiO₂ nanocatalyst for the photocatalytic and sonophotocatalytic degradation of chlorpyrifos. *Can. J. Chem. Eng.* **2022**, *100*, 451–464. [[CrossRef](#)]
24. Nekooie, R.; Shamspur, T.; Mostafavi, A. Novel CuO/TiO₂/PANI nanocomposite: Preparation and photocatalytic investigation for chlorpyrifos degradation in water under visible light irradiation. *J. Photochem. Photobiol. A* **2021**, *407*, 113038. [[CrossRef](#)]
25. Anirudhan, T.S.; Manjusha, V.; Shainy, F. Magnetically retrievable cysteine modified graphene oxide@nickelferrite@titanium dioxide photocatalyst for the effective degradation of chlorpyrifos from aqueous solutions. *Environ. Technol. Innov.* **2021**, *23*, 101633. [[CrossRef](#)]
26. Ikrari, K.I.; Hasbullah, H.; Salleh, W.N.W.; Nakagawa, K.; Yoshioka, T. Photocatalytic membrane technologies for removal of recalcitrant pollutants. *Mater. Today Proc.* **2022**, *65*, 3101–3108. [[CrossRef](#)]
27. Zuraimi, M.S.; Magee, R.J.; Won, D.Y.; Nong, G.; Arsenault, C.D.; Yang, W.; So, S.; Nilsson, G.; Abebe, L.; Alliston, C. Performance of sorption- and photocatalytic oxidation-based indoor passive panel technologies. *Build. Environ.* **2018**, *135*, 85–93. [[CrossRef](#)]
28. Chong, M.N.; Jin, B.; Chow, C.W.K.; Saint, C. Recent developments in photocatalytic water treatment technology: A review. *Water Res.* **2010**, *44*, 2997–3027. [[CrossRef](#)]
29. Sun, Y.; Zhang, W.; Li, Q.; Liu, H.; Wang, X. Preparations and applications of zinc oxide based photocatalytic materials. *Adv. Sens. Energy Mater.* **2023**, *2*, 100069. [[CrossRef](#)]
30. Lee, S.F.; Jimenez-Relinque, E.; Martinez, I.; Castellote, M. Effects of Mott-Schottky Frequency Selection and Other Controlling Factors on Flat-Band Potential and Band-Edge Position Determination of TiO₂. *Catalysts* **2023**, *13*, 1000. [[CrossRef](#)]
31. Lee, S.F.; Jimenez-Relinque, E.; Martinez, I.; Castellote, M. Photoelectrochemical global approach to the behaviour of nanostructured anatase under different irradiation conditions. *Catal. Today* **2022**, *397*, 286–295. [[CrossRef](#)]
32. Supin, K.K.; Namboothiri, P.P.M.; Vasundhara, M. Enhanced photocatalytic activity in ZnO nanoparticles developed using novel *Lepidagathis ananthapuramensis* leaf extract. *RSC Adv.* **2023**, *13*, 1497–1515. [[CrossRef](#)]

33. Ziental, D.; Czarczynska-Goslinska, B.; Mlynarczyk, D.T.; Glowacka-Sobotta, A.; Stanisz, B.; Goslinski, T.; Sobotta, L. Titanium Dioxide Nanoparticles: Prospects and Applications in Medicine. *Nanomaterials* **2020**, *10*, 387. [[CrossRef](#)] [[PubMed](#)]
34. Ghosal, K.; Agatemor, C.; Spitalsky, Z.; Thomas, S.; Kny, E. Electrospinning tissue engineering and wound dressing scaffolds from polymer-titanium dioxide nanocomposites. *Chem. Eng. J.* **2019**, *358*, 1262–1278. [[CrossRef](#)]
35. Lu, P.J.; Huang, S.C.; Chen, Y.P.; Chiueh, L.C.; Shih, D.Y.C. Analysis of titanium dioxide and zinc oxide nanoparticles in cosmetics. *J. Food Drug Anal.* **2015**, *23*, 587–594. [[CrossRef](#)] [[PubMed](#)]
36. Dimapilis, E.A.S.; Hsu, C.S.; Mendoza, R.M.O.; Lu, M.C. Zinc oxide nanoparticles for water disinfection. *Sustain. Environ. Res.* **2018**, *28*, 47–56. [[CrossRef](#)]
37. Kolodziejczak-Radzimska, A.; Jesionowski, T. Zinc Oxide-From Synthesis to Application: A Review. *Materials* **2014**, *7*, 2833–2881. [[CrossRef](#)] [[PubMed](#)]
38. Roohandeh, L.; Hakimyfar, A.; Samimifar, M. High efficient solar light photocatalytic degradation of malachite green by solid state synthesized $\text{Bi}_2\text{Sn}_2\text{O}_7$ and $\text{Bi}_2\text{M}_x\text{Sn}_2\text{O}_7$ ($\text{M} = \text{Y}^{3+}$, Eu^{3+} , Gd^{3+} and Yb^{3+}) nanomaterials. *J. Nanoanal.* **2020**, *7*, 240–247.
39. Abe, R.; Higashi, M.; Zou, Z.G.; Sayama, K.; Abe, Y. Photocatalytic water splitting into H_2 and O_2 over $\text{R}_2\text{Ti}_2\text{O}_7$ ($\text{R} = \text{Y}$, rare earth) with pyrochlore structure. *Chem. Lett.* **2004**, *33*, 954–955. [[CrossRef](#)]
40. Luan, J.F.; Hu, Z.T. Synthesis, Property Characterization, and Photocatalytic Activity of Novel Visible Light-Responsive Photocatalyst $\text{Fe}_2\text{BiSbO}_7$. *Int. J. Photoenergy* **2012**, *2012*, 301954. [[CrossRef](#)]
41. Devi, V.R.; Ravi, G.; Velchuri, R.; Muniratnam, N.R.; Prasad, G.; Vithal, M. Preparation, Characterization, Photocatalytic Activity and Conductivity Studies of YLnTi_2O_7 ($\text{Ln} = \text{Nd}$, Sm , Eu and Gd). *Trans. Indian Ceram. Soc.* **2013**, *72*, 241–251. [[CrossRef](#)]
42. Zhang, S.; Wen, Z.; Zhao, Y.; Li, G.; Li, Z. Preparation, Characterization of $\text{A}_2\text{Ce}_2\text{O}_7$ ($\text{A} = \text{La}$ and Gd) and Their Photo-Catalytic Properties. *Energy Environ. Focus* **2015**, *4*, 324–329. [[CrossRef](#)]
43. Li, J.; Zhang, X.; Ai, Z.; Jia, F.; Zhang, L.; Lin, J. Efficient Visible Light Degradation of Rhodamine B by a Photo-Electrochemical Process Based on a Bi_2WO_6 Nanoplate Film Electrode. *J. Phys. Chem. C* **2007**, *111*, 6832–6836. [[CrossRef](#)]
44. Zhao, C.R.; Cai, L.Y.; Wang, K.Q.; Li, B.X.; Yuan, S.D.; Zeng, Z.H.; Zhao, L.H.; Wu, Y.; He, Y.M. Novel $\text{Bi}_2\text{WO}_6/\text{ZnSnO}_3$ heterojunction for the ultrasonic-vibration-driven piezocatalytic degradation of RhB. *Environ. Pollut.* **2023**, *319*, 120982. [[CrossRef](#)] [[PubMed](#)]
45. Zhu, Y.Y.; Wang, Y.J.; Ling, Q.; Zhu, Y.F. Enhancement of full-spectrum photocatalytic activity over $\text{BiPO}_4/\text{Bi}_2\text{WO}_6$ composites. *Appl. Catal. B Environ.* **2017**, *200*, 222–229. [[CrossRef](#)]
46. Tian, Y.L.; Chang, B.B.; Lu, J.L.; Fu, J.; Xi, F.N.; Dong, X.P. Hydrothermal Synthesis of Graphitic Carbon Nitride- Bi_2WO_6 Heterojunctions with Enhanced Visible Light Photocatalytic Activities. *ACS Appl. Mater. Interfaces* **2013**, *5*, 7079–7085. [[CrossRef](#)]
47. Zhao, Y.; Wang, Y.; Liu, E.; Fan, J.; Hu, X. Bi_2WO_6 nanoflowers: An efficient visible light photocatalytic activity for ceftriaxone sodium degradation. *Appl. Surf. Sci.* **2018**, *436*, 854–864. [[CrossRef](#)]
48. Lai, M.T.L.; Lai, C.W.; Lee, K.M.; Chook, S.W.; Yang, T.C.K.; Chong, S.H.; Juan, J.C. Facile one-pot solvothermal method to synthesize solar active Bi_2WO_6 for photocatalytic degradation of organic dye. *J. Alloys Compd.* **2019**, *801*, 502–510. [[CrossRef](#)]
49. Zou, Z.G.; Ye, J.H.; Abe, R.; Arakawa, H. Photocatalytic decomposition of water with $\text{Bi}_2\text{InNbO}_7$. *Catal. Lett.* **2000**, *68*, 235–239. [[CrossRef](#)]
50. Zuo, G.; Ma, S.; Yin, Z.; Chen, W.; Wang, Y.; Ji, Q.; Xian, Q.; Yang, S.; He, H. Z-Scheme Modulated Charge Transfer on $\text{InVO}_4/\text{ZnIn}_2\text{S}_4$ for Durable Overall Water Splitting. *Small* **2023**, *19*, 2207031. [[CrossRef](#)]
51. Wang, Q.; Li, Y.; Huang, F.; Song, S.; Ai, G.; Xin, X.; Zhao, B.; Zheng, Y.; Zhang, Z. Recent Advances in g- C_3N_4 -Based Materials and Their Application in Energy and Environmental Sustainability. *Molecules* **2023**, *28*, 432. [[CrossRef](#)] [[PubMed](#)]
52. Yu, Y.; Cao, C.Y.; Liu, H.; Li, P.; Wei, F.F.; Jiang, Y.; Song, W.G. A Bi/BiOCl heterojunction photocatalyst with enhanced electron-hole separation and excellent visible light photodegrading activity. *J. Mater. Chem. A* **2014**, *2*, 1677–1681. [[CrossRef](#)]
53. Wang, W.J.; Yu, J.C.; Xia, D.H.; Wong, P.K.; Li, Y.C. Graphene and g- C_3N_4 Nanosheets Cowrapped Elemental α -Sulfur As a Novel Metal-Free Heterojunction Photocatalyst for Bacterial Inactivation under Visible-Light. *Environ. Sci. Technol.* **2013**, *47*, 8724–8732. [[CrossRef](#)] [[PubMed](#)]
54. Shen, T.; Shi, X.K.; Guo, J.X.; Li, J.; Yuan, S.D. Photocatalytic removal of NO by light-driven $\text{Mn}_3\text{O}_4/\text{BiOCl}$ heterojunction photocatalyst: Optimization and mechanism. *Chem. Eng. J.* **2021**, *408*, 128014. [[CrossRef](#)]
55. Jiang, T.G.; Wang, K.; Guo, T.; Wu, X.Y.; Zhang, G.K. Fabrication of Z-scheme $\text{MoO}_3/\text{Bi}_2\text{O}_4$ heterojunction photocatalyst with enhanced photocatalytic performance under visible light irradiation. *Chin. J. Catal.* **2020**, *41*, 161–169. [[CrossRef](#)]
56. Liu, Y.; Kong, J.J.; Yuan, J.L.; Zhao, W.; Zhu, X.; Sun, C.; Xie, J.M. Enhanced photocatalytic activity over flower-like sphere $\text{Ag}/\text{Ag}_2\text{CO}_3/\text{BiVO}_4$ plasmonic heterojunction photocatalyst for tetracycline degradation. *Chem. Eng. J.* **2018**, *331*, 242–254. [[CrossRef](#)]
57. Sohrabian, M.; Mahdikhah, V.; Alimohammadi, E.; Sheibani, S. Improved photocatalytic performance of SrTiO_3 through a Z-scheme polymeric-perovskite heterojunction with g- C_3N_4 and plasmonic resonance of Ag mediator. *Appl. Surf. Sci.* **2023**, *618*, 156682. [[CrossRef](#)]
58. Zhu, B.C.; Cheng, B.; Fan, J.J.; Ho, W.K.; Yu, J.G. g- C_3N_4 -Based 2D/2D Composite Heterojunction Photocatalyst. *Small Struct.* **2021**, *2*, 2100086. [[CrossRef](#)]
59. Xu, H.; Xu, Y.G.; Li, H.M.; Xia, J.X.; Xiong, J.; Yin, S.; Huang, C.J.; Wan, H.L. Synthesis, characterization and photocatalytic property of $\text{AgBr}/\text{BiPO}_4$ heterojunction photocatalyst. *Dalton Trans.* **2012**, *41*, 3387–3394. [[CrossRef](#)]

60. Wen, X.J.; Qian, L.; Lv, X.X.; Sun, J.; Guo, J.; Fei, Z.H.; Niu, C.G. Photocatalytic degradation of sulfamethazine using a direct Z-scheme AgI/Bi₄V₂O₁₁ photocatalyst: Mineralization activity, degradation pathways and promoted charge separation mechanism. *J. Hazard. Mater.* **2020**, *385*, 121508. [CrossRef]
61. Pathania, D.; Sharma, A.; Kumar, S.; Srivastava, A.K.; Kumar, A.; Singh, L. Bio-synthesized Cu-ZnO hetero-nanostructure for catalytic degradation of organophosphate chlorpyrifos under solar illumination. *Chemosphere* **2021**, *277*, 130315. [CrossRef] [PubMed]
62. Farner Budariz, J.; Cooper, E.M.; Gardner, C.; Hodzic, E.; Ferguson, P.L.; Gunsch, C.K.; Wiesner, M.R. Chlorpyrifos degradation via photoreactive TiO₂ nanoparticles: Assessing the impact of a multi-component degradation scenario. *J. Hazard. Mater.* **2019**, *372*, 61–68. [CrossRef] [PubMed]
63. Wang, J.H.; Zou, Z.G.; Ye, J.H. Synthesis, structure and photocatalytic property of a new hydrogen evolving photocatalyst Bi₂InTaO₇. In *Functionally Graded Materials VII*; Pan, W., Gong, J., Zhang, L., Chen, L., Eds.; Trans Tech Publications Ltd.: Zurich-Uetikon, Switzerland, 2003; Volume 423-4, pp. 485–490.
64. Muniz, F.T.L.; Miranda, M.A.R.; Morilla dos Santos, C.; Sasaki, J.M. The Scherrer equation and the dynamical theory of X-ray diffraction. *Acta Crystallogr. Sect. A Found. Adv.* **2016**, *72*, 385–390. [CrossRef] [PubMed]
65. Hargreaves, J.S.J. Some considerations related to the use of the Scherrer equation in powder X-ray diffraction as applied to heterogeneous catalysts. *Catal. Struct. React.* **2016**, *2*, 33–37. [CrossRef]
66. Mustapha, S.; Ndamitso, M.M.; Abdulkareem, A.S.; Tijani, J.O.; Shuaib, D.T.; Mohammed, A.K.; Sumaila, A. Comparative study of crystallite size using Williamson-Hall and Debye-Scherrer plots for ZnO nanoparticles. *Adv. Nat. Sci. Nanosci. Nanotechnol.* **2019**, *10*, 045013. [CrossRef]
67. Bibi, H.; Iqbal, M.; Wahab, H.; Öztürk, M.; Ke, F.; Iqbal, Z.; Khan, M.I.; Alghanem, S.M. Green synthesis of multifunctional carbon coated copper oxide nanosheets and their photocatalytic and antibacterial activities. *Sci. Rep.* **2021**, *11*, 10781. [CrossRef] [PubMed]
68. Lok, R.; Budak, E.; Yilmaz, E. Structural characterization and electrical properties of Nd₂O₃ by sol-gel method. *J. Mater. Sci.-Mater. Electron.* **2020**, *31*, 3111–3118. [CrossRef]
69. Yuvakkumar, R.; Hong, S.I. Nd₂O₃: Novel synthesis and characterization. *J. Sol-Gel Sci. Technol.* **2015**, *73*, 511–517. [CrossRef]
70. Garbout, A.; Ben Taazayet-Belgacem, I.; Férid, M. Structural, FT-IR, XRD and Raman scattering of new rare-earth-titanate pyrochlore-type oxides LnEuTi₂O₇ (Ln = Gd, Dy). *J. Alloys Compd.* **2013**, *573*, 43–52. [CrossRef]
71. Bosca, M.; Pop, L.; Borodi, G.; Pascuta, P.; Culea, E. XRD and FTIR structural investigations of erbium-doped bismuth-lead-silver glasses and glass ceramics. *J. Alloys Compd.* **2009**, *479*, 579–582. [CrossRef]
72. Pascuta, P.; Culea, E. FTIR spectroscopic study of some bismuth germanate glasses containing gadolinium ions. *Mater. Lett.* **2008**, *62*, 4127–4129. [CrossRef]
73. Kaviyarasu, K.; Sajan, D.; Devarajan, P.A. A rapid and versatile method for solvothermal synthesis of Sb₂O₃ nanocrystals under mild conditions. *Appl. Nanosci.* **2012**, *3*, 529–533. [CrossRef]
74. Rada, S.; Rus, L.; Rada, M.; Zagrai, M.; Culea, E.; Rusu, T. Compositional dependence of structure, optical and electrochemical properties of antimony(III) oxide doped lead glasses and vitroceramics. *Ceram. Int.* **2014**, *40*, 15711–15716. [CrossRef]
75. Duan, F.; Zhang, Q.; Shi, D.; Chen, M. Enhanced visible light photocatalytic activity of Bi₂WO₆ via modification with polypyrrole. *Appl. Surf. Sci.* **2013**, *268*, 129–135. [CrossRef]
76. Janani, B.; Okla, M.K.; Abdel-Maksoud, M.A.; Abdelgawad, H.; Thomas, A.M.; Raju, L.L.; Al-Qahtani, W.H.; Khan, S.S. CuO loaded ZnS nanoflower entrapped on PVA-chitosan matrix for boosted visible light photocatalysis for tetracycline degradation and anti-bacterial application. *J. Environ. Manag.* **2022**, *306*, 114396. [CrossRef] [PubMed]
77. Li, R.; Cai, M.; Xie, Z.; Zhang, Q.; Zeng, Y.; Liu, H.; Liu, G.; Lv, W. Construction of heterostructured CuFe₂O₄/g-C₃N₄ nanocomposite as an efficient visible light photocatalyst with peroxydisulfate for the organic oxidation. *Appl. Catal. B Environ.* **2019**, *244*, 974–982. [CrossRef]
78. Cheng, T.; Gao, H.; Liu, G.; Pu, Z.; Wang, S.; Yi, Z.; Wu, X.; Yang, H. Preparation of core-shell heterojunction photocatalysts by coating CdS nanoparticles onto Bi₄Ti₃O₁₂ hierarchical microspheres and their photocatalytic removal of organic pollutants and Cr(VI) ions. *Colloids Surf. A Physicochem. Eng. Asp.* **2022**, *633*, 127918. [CrossRef]
79. Al-Oweini, R.; El-Rassy, H. Synthesis and characterization by FTIR spectroscopy of silica aerogels prepared using several Si(OR)₄ and R''Si(OR')₃ precursors. *J. Mol. Struct.* **2009**, *919*, 140–145. [CrossRef]
80. Isari, A.A.; Hayati, F.; Kakavandi, B.; Rostami, M.; Motevassel, M.; Dehghanifard, E. N, Cu co-doped TiO₂@functionalized SWCNT photocatalyst coupled with ultrasound and visible-light: An effective sono-photocatalysis process for pharmaceutical wastewaters treatment. *Chem. Eng. J.* **2020**, *392*, 123685. [CrossRef]
81. Shao, B.; Liu, X.; Liu, Z.; Zeng, G.; Liang, Q.; Liang, C.; Cheng, Y.; Zhang, W.; Liu, Y.; Gong, S. A novel double Z-scheme photocatalyst Ag₃PO₄/Bi₂S₃/Bi₂O₃ with enhanced visible-light photocatalytic performance for antibiotic degradation. *Chem. Eng. J.* **2019**, *368*, 730–745. [CrossRef]
82. Zhang, Y.; Bhadbhade, M.; Scales, N.; Karatchevtseva, I.; Price, J.R.; Lu, K.; Lumpkin, G.R. Dysprosium complexes with mono-/di-carboxylate ligands—From simple dimers to 2D and 3D frameworks. *J. Solid State Chem.* **2014**, *219*, 1–8. [CrossRef]
83. Khadraoui, Z.; Bouzidi, C.; Horchani-Naifer, K.; Ferid, M. Crystal structure, energy band and optical properties of dysprosium monophosphate DyPO₄. *J. Alloys Compd.* **2014**, *617*, 281–286. [CrossRef]

84. Refat, M.S.; Elsabay, K.M. Infrared spectra, Raman laser, XRD, DSC/TGA and SEM investigations on the preparations of selenium metal, (Sb₂O₃, Ga₂O₃, SnO and HgO) oxides and lead carbonate with pure grade using acetamide precursors. *Bull. Mater. Sci.* **2011**, *34*, 873–881. [[CrossRef](#)]
85. Gilliam, S.J.; Jensen, J.O.; Banerjee, A.; Zeroka, D.; Kirkby, S.J.; Merrow, C.N. A theoretical and experimental study of Sb₄O₆: Vibrational analysis, infrared, and Raman spectra. *Spectrochim. Acta A Mol. Biomol. Spectrosc.* **2004**, *60*, 425–434. [[CrossRef](#)] [[PubMed](#)]
86. Serqueira, E.O.; Dantas, N.O.; Anjos, V.; Bell, M.J.V. Raman Spectroscopy of SiO₂–Na₂O–Al₂O₃–B₂O₃ glass doped with Nd³⁺ and CdS nanocrystals. *J. Alloys Compd.* **2014**, *582*, 730–733. [[CrossRef](#)]
87. Xiang, Y.; Ju, P.; Wang, Y.; Sun, Y.; Zhang, D.; Yu, J. Chemical etching preparation of the Bi₂WO₆/BiOI p–n heterojunction with enhanced photocatalytic antifouling activity under visible light irradiation. *Chem. Eng. J.* **2016**, *288*, 264–275. [[CrossRef](#)]
88. Chahine, A.; Et-tabirou, M.; Pascal, J.L. FTIR and Raman spectra of the Na₂O–CuO–Bi₂O₃–P₂O₅ glasses. *Mater. Lett.* **2004**, *58*, 2776–2780. [[CrossRef](#)]
89. Nowak, M.; Kauch, B.; Szperlich, P. Determination of energy band gap of nanocrystalline SbSI using diffuse reflectance spectroscopy. *Rev. Sci. Instrum.* **2009**, *80*, 046107. [[CrossRef](#)]
90. Zhou, F.; Kang, K.; Maxisch, T.; Ceder, G.; Morgan, D. The electronic structure and band gap of LiFePO₄ and LiMnPO₄. *Solid State Commun.* **2004**, *132*, 181–186. [[CrossRef](#)]
91. Butler, M.A.; Ginley, D.S.; Eibschutz, M. Photoelectrolysis with YFeO₃ electrodes. *J. Appl. Phys.* **1977**, *48*, 3070–3072. [[CrossRef](#)]
92. Tauc, J.; Grigorovici, R.; Vancu, A. Optical properties and electronic structure of amorphous germanium. *Phys. Status Solidi* **1966**, *15*, 627–637. [[CrossRef](#)]
93. Makula, P.; Pacia, M.; Macyk, W. How To Correctly Determine the Band Gap Energy of Modified Semiconductor Photocatalysts Based on UV-Vis Spectra. *J. Phys. Chem. Lett.* **2018**, *9*, 6814–6817. [[CrossRef](#)] [[PubMed](#)]
94. Liu, X.; Fan, H.Q. Theoretical studies on electronic structure and optical properties of Bi₂WO₆. *Optik* **2018**, *158*, 962–969. [[CrossRef](#)]
95. Saeed, M.; ul Haq, A.; Muneer, M.; Ahmad, A.; Bokhari, T.H.; Sadiq, Q. Synthesis and characterization of Bi₂O₃ and Ag–Bi₂O₃ and evaluation of their photocatalytic activities towards photodegradation of crystal violet dye. *Phys. Scr.* **2021**, *96*, 125707. [[CrossRef](#)]
96. Liu, B.Y.; Du, J.Y.; Ke, G.L.; Jia, B.; Huang, Y.J.; He, H.C.; Zhou, Y.; Zou, Z.G. Boosting O₂ Reduction and H₂O Dehydrogenation Kinetics: Surface N-Hydroxymethylation of g-C₃N₄ Photocatalysts for the Efficient Production of H₂O₂. *Adv. Funct. Mater.* **2022**, *32*, 2111125. [[CrossRef](#)]
97. Liu, C.; Feng, Y.; Han, Z.T.; Sun, Y.; Wang, X.Q.; Zhang, Q.F.; Zou, Z.G. Z-scheme N-doped K₄Nb₆O₁₇/g-C₃N₄ heterojunction with superior visible-light-driven photocatalytic activity for organic pollutant removal and hydrogen production. *Chin. J. Catal.* **2021**, *42*, 164–174. [[CrossRef](#)]
98. Wang, L.; Wang, J.; Fei, Y.; Cheng, H.; Pan, H.; Wu, C. Ag₃PO₄/Bi₂WO₆ Heterojunction Photocatalyst with Remarkable Visible-Light-Driven Catalytic Activity. *Crystals* **2023**, *13*, 1531. [[CrossRef](#)]
99. Zhang, H.; Fan, Z.; Chai, Q.; Li, J. Facile Synthesis of a Bi₂WO₆/BiO_{2-x} Heterojunction for Efficient Photocatalytic Degradation of Ciprofloxacin under Visible Light Irradiation. *Catalysts* **2023**, *13*, 469. [[CrossRef](#)]
100. Liu, A.; Hu, J.; He, J.; Huang, X.; Hu, N.; Li, Y.; Huang, Q.; Guo, S.; Liu, X.; Yang, Z.; et al. Direct Z-scheme hierarchical heterostructures of oxygen-doped g-C₃N₄/In₂S₃ with efficient photocatalytic Cr(vi) reduction activity. *Catal. Sci. Technol.* **2021**, *11*, 7963–7972. [[CrossRef](#)]
101. Ashfaq, M.; Ali, A.; Abbood, N.K.; Panchal, S.; Akram, N.; Saeed, M.; Doshi, O.P.; Ali, F.; Muhammad, S.; Sameeh, M.Y.; et al. Enhanced Photocatalytic Activity of the Bi₂O₃–NiO Heterojunction for the Degradation of Methyl Orange under Irradiation of Sunlight. *Water* **2023**, *15*, 3182. [[CrossRef](#)]
102. Al Bawab, A.; Abu-Dalo, M.; Khalaf, A.; Abu-Dalo, D. Olive Mill Wastewater (OMW) Treatment Using Photocatalyst Media. *Catalysts* **2022**, *12*, 539. [[CrossRef](#)]
103. Cabir, B.; Yurderi, M.; Caner, N.; Agirtas, M.S.; Zahmakiran, M.; Kaya, M. Methylene blue photocatalytic degradation under visible light irradiation on copper phthalocyanine-sensitized TiO₂ nanopowders. *Mater. Sci. Eng. B* **2017**, *224*, 9–17. [[CrossRef](#)]
104. Morrison, C.; Sun, H.; Yao, Y.; Loomis, R.A.; Buhro, W.E. Methods for the ICP-OES Analysis of Semiconductor Materials. *Chem. Mater.* **2020**, *32*, 1760–1768. [[CrossRef](#)]
105. Taleghani, M.S.; Tabrizi, N.S.; Sangpour, P. Enhanced visible-light photocatalytic activity of titanium dioxide doped CNT-C aerogel. *Chem. Eng. Res. Des.* **2022**, *179*, 162–174. [[CrossRef](#)]
106. Senasu, T.; Lorwanishpaisarn, N.; Hemavibool, K.; Nijpanich, S.; Chanlek, N.; Nanan, S. Construction of g-C₃N₄/BiOCl/CdS heterostructure photocatalyst for complete removal of oxytetracycline antibiotic in wastewater. *Sep. Purif. Technol.* **2023**, *306*, 122735. [[CrossRef](#)]
107. Sabzehparvar, M.; Kiani, F.; Tabrizi, N.S. Mesoporous-assembled TiO₂–NiO–Ag nanocomposites with p–n/Schottky heterojunctions for enhanced photocatalytic performance. *J. Alloys Compd.* **2021**, *876*, 160133. [[CrossRef](#)]
108. Esfandian, H.; Rostamnejad Cherati, M.; Khatirian, M. Electrochemical behavior and photocatalytic performance of chlorpyrifos pesticide decontamination using Ni-doped ZnO–TiO₂ nanocomposite. *Inorg. Chem. Commun.* **2024**, *159*, 111750. [[CrossRef](#)]
109. Khan, S.H.; Pathak, B.; Fulekar, M.H. Synthesis, characterization and photocatalytic degradation of chlorpyrifos by novel Fe: ZnO nanocomposite material. *Nanotechnol. Environ. Eng.* **2018**, *3*, 13. [[CrossRef](#)]
110. Luan, J.; Wei, Z.; Niu, B.; Yang, G.; Huang, C.; Ma, B.; Liu, W. Synthesis, Property Characterization and Photocatalytic Activity of the Ag₃PO₄/Gd₂BiTaO₇ Heterojunction Catalyst under Visible Light Irradiation. *Catalysts* **2021**, *12*, 22. [[CrossRef](#)]

111. Zafar, Z.; Fatima, R.; Kim, J.-O. Experimental studies on water matrix and influence of textile effluents on photocatalytic degradation of organic wastewater using Fe–TiO₂ nanotubes: Towards commercial application. *Environ. Res.* **2021**, *197*, 111120. [[CrossRef](#)]
112. Cruz, M.; Gomez, C.; Duran-Valle, C.J.; Pastrana-Martínez, L.M.; Faria, J.L.; Silva, A.M.T.; Faraldos, M.; Bahamonde, A. Bare TiO₂ and graphene oxide TiO₂ photocatalysts on the degradation of selected pesticides and influence of the water matrix. *Appl. Surf. Sci.* **2017**, *416*, 1013–1021. [[CrossRef](#)]
113. Zhuang, Y.; Luan, J. Improved photocatalytic property of peony-like InOOH for degrading norfloxacin. *Chem. Eng. J.* **2020**, *382*, 122770. [[CrossRef](#)]
114. Balakrishnan, G.; Velavan, R.; Mujasam Batoo, K.; Raslan, E.H. Microstructure, optical and photocatalytic properties of MgO nanoparticles. *Results Phys.* **2020**, *16*, 103013. [[CrossRef](#)]
115. Liqiang, J.; Yichun, Q.; Baiqi, W.; Shudan, L.; Baojiang, J.; Libin, Y.; Wei, F.; Honggang, F.; Jiazhong, S. Review of photoluminescence performance of nano-sized semiconductor materials and its relationships with photocatalytic activity. *Sol. Energy Mater. Sol. Cells* **2006**, *90*, 1773–1787. [[CrossRef](#)]
116. Chen, J.; Zhao, X.; Kim, S.G.; Park, N.G. Multifunctional Chemical Linker Imidazoleacetic Acid Hydrochloride for 21% Efficient and Stable Planar Perovskite Solar Cells. *Adv. Mater.* **2019**, *31*, 1902902. [[CrossRef](#)] [[PubMed](#)]
117. Gao, Z.W.; Wang, Y.; Ouyang, D.; Liu, H.; Huang, Z.F.; Kim, J.; Choy, W.C.H. Triple Interface Passivation Strategy-Enabled Efficient and Stable Inverted Perovskite Solar Cells. *Small Methods* **2020**, *4*, 2000478. [[CrossRef](#)]
118. Chen, J.; Kim, S.-G.; Ren, X.; Jung, H.S.; Park, N.-G. Effect of bidentate and tridentate additives on the photovoltaic performance and stability of perovskite solar cells. *J. Mater. Chem. A* **2019**, *7*, 4977–4987. [[CrossRef](#)]
119. Ma, Q.; Kumar, R.K.; Xu, S.Y.; Koppens, F.H.L.; Song, J.C.W. Photocurrent as a multiphysics diagnostic of quantum materials. *Nat. Rev. Phys.* **2023**, *5*, 170–184. [[CrossRef](#)]
120. Cheng, Y.X.; Ye, J.H.; Lai, L.; Fang, S.; Guo, D.Y. Ambipolarity Regulation of Deep-UV Photocurrent by Controlling Crystalline Phases in Ga₂O₃ Nanostructure for Switchable Logic Applications. *Adv. Electron. Mater.* **2023**, *9*, 2201216. [[CrossRef](#)]
121. Bredar, A.R.C.; Chown, A.L.; Burton, A.R.; Farnum, B.H. Electrochemical Impedance Spectroscopy of Metal Oxide Electrodes for Energy Applications. *ACS Appl. Energy Mater.* **2020**, *3*, 66–98. [[CrossRef](#)]
122. Behera, A.; Mansingh, S.; Das, K.K.; Parida, K. Synergistic ZnFe₂O₄-carbon allotropes nanocomposite photocatalyst for norfloxacin degradation and Cr (VI) reduction. *J. Colloid Interface Sci.* **2019**, *544*, 96–111. [[CrossRef](#)] [[PubMed](#)]
123. Annadi, A.; Gong, H. Success in both p-type and n-type of a novel transparent AgCuI alloy semiconductor system for homojunction devices. *Appl. Mater. Today* **2020**, *20*, 100703. [[CrossRef](#)]
124. Xu, S.; Gong, S.; Jiang, H.; Shi, P.; Fan, J.; Xu, Q.; Min, Y. Z-scheme heterojunction through interface engineering for broad spectrum photocatalytic water splitting. *Appl. Catal. B* **2020**, *267*, 118661. [[CrossRef](#)]
125. Cheng, T.; Gao, H.; Sun, X.; Xian, T.; Wang, S.; Yi, Z.; Liu, G.; Wang, X.; Yang, H. An excellent Z-scheme Ag₂MoO₄/Bi₄Ti₃O₁₂ heterojunction photocatalyst: Construction strategy and application in environmental purification. *Adv. Powder Technol.* **2021**, *32*, 951–962. [[CrossRef](#)]
126. Huang, W.; Li, Y.F.; Fu, Q.M.; Chen, M. Fabrication of a novel biochar decorated nano-flower-like MoS₂ nanomaterial for the enhanced photodegradation activity of ciprofloxacin: Performance and mechanism. *Mater. Res. Bull.* **2022**, *147*, 111650. [[CrossRef](#)]
127. Yan, S.W.; Yang, J.; Li, Y.; Jia, X.H.; Song, H.J. One-step synthesis of ZnS/BiOBr photocatalyst to enhance photodegradation of tetracycline under full spectral irradiation. *Mater. Lett.* **2020**, *276*, 128232. [[CrossRef](#)]
128. Zhang, W.; Zhou, L.; Shi, J.; Deng, H.P. Synthesis of Ag₃PO₄/G-C₃N₄ Composite with Enhanced Photocatalytic Performance for the Photodegradation of Diclofenac under Visible Light Irradiation. *Catalysts* **2018**, *8*, 45. [[CrossRef](#)]
129. Zhang, J.L.; Ma, Z. Ag₃VO₄/AgI composites for photocatalytic degradation of dyes and tetracycline hydrochloride under visible light. *Mater. Lett.* **2018**, *216*, 216–219. [[CrossRef](#)]
130. Zhang, J.F.; Hu, Y.F.; Jiang, X.L.; Chen, S.F.; Meng, S.G.; Fu, X.L. Design of a direct Z-scheme photocatalyst: Preparation and characterization of Bi₂O₃/g-C₃N₄ with high visible light activity. *J. Hazard. Mater.* **2014**, *280*, 713–722. [[CrossRef](#)]
131. Zuo, C.; Tai, X.S.; Jiang, Z.Y.; Liu, M.F.; Jiang, J.H.; Su, Q.; Yan, X.Y. S-Scheme 2D/2D Heterojunction of ZnTiO₃ Nanosheets/Bi₂WO₆ Nanosheets with Enhanced Photoelectrocatalytic Activity for Phenol Wastewater under Visible Light. *Molecules* **2023**, *28*, 3495. [[CrossRef](#)]
132. Tamtam, M.R.; Koutavarapu, R.; Choi, G.S.; Shim, J. Z-Scheme Photocatalytic Degradation of Potassium Butyl Xanthate by a 2D/2D Heterojunction of Bi₂WO₆ Using MoS₂ as a Co-Catalyst. *Catalysts* **2023**, *13*, 1238. [[CrossRef](#)]

133. Majhi, D.; Bhoi, Y.P.; Samal, P.K.; Mishra, B.G. Morphology controlled synthesis and photocatalytic study of novel CuS-Bi₂O₂CO₃ heterojunction system for chlorpyrifos degradation under visible light illumination. *Appl. Surf. Sci.* **2018**, *455*, 891–902. [[CrossRef](#)]
134. Samy, M.; Ibrahim, M.G.; Gar Alalm, M.; Fujii, M.; Diab, K.E.; ElKady, M. Innovative photocatalytic reactor for the degradation of chlorpyrifos using a coated composite of ZrV₂O₇ and graphene nano-platelets. *Chem. Eng. J.* **2020**, *395*, 124974. [[CrossRef](#)]

Disclaimer/Publisher's Note: The statements, opinions and data contained in all publications are solely those of the individual author(s) and contributor(s) and not of MDPI and/or the editor(s). MDPI and/or the editor(s) disclaim responsibility for any injury to people or property resulting from any ideas, methods, instructions or products referred to in the content.